MECHANICS AND DEFORMATION OF POLYMER KIRIGAMI STRUCTURES

A Thesis

by

KIAN BASHANDEH KHODAEI NAEINI

Submitted to the Office of Graduate and Professional Studies of
Texas A&M University
in partial fulfillment of the requirements for the degree of

MASTER OF SCIENCE

Chair of Committee,	Andreas A. Polycarpou
Committee Members,	M. Cynthia Hipwell
	Matt Pharr
	Mohammad Naraghi
Head of Department,	Andreas A. Polycarpou

December 2020

Major Subject: Mechanical Engineering

ABSTRACT

Recent advances in the assembly of three-dimensional (3D) structures driven by compressive buckling of 2D precursors have provided an opportunity to exploit the capability in a broad range of engineering applications with complex geometries and a span of length scales from sub-micron to macro scales. These applications include but not limited to microelectromechanical systems, energy storage, and wearable electronic devices. The present work is dedicated to study the fabrication of flexible 3D kirigami-inspired polymer-based structures using mechanically-guided 3D micro-assembly. The mechanical response of assembled 3D buckled kirigami structures were investigated through mechanical cyclic and single loading compression at room and elevated temperatures.

Although a variety of 3D structures with different geometrical and material arrangements were fabricated already, their mechanical response to applied load is still unknown. In this thesis, the mechanics of these kirigami structures were studied using experimental in-situ scanning electron microscopy (SEM) flat punch compression. Computational modeling was conducted to support the experimental findings and to investigate and understand the deformation and fracture of the structures.

Our findings revealed that the load-bearing capacity, resilience, and stability under deformation were largely affected by structures' geometry. Furthermore, the structures with defects were also found to achieve stable hysteretic cycling with steady-state mechanical response after a number of cycles.

The information presented in this thesis is of great interest in understanding the mechanics of 3D polymer-based structures. The work is expected to contribute to the current and future research on the development of flexible and stretchable biomedical devices as in tissue repair and vascular stents, as well as adaptive and deployable structures in aerospace engineering and wearable electronics.

ACKNOWLEDGEMENTS

I would like to thank my advisor, Professor Andreas Polycarpou, for his valuable guidance, support, and encouragement throughout this research project.

I would like to thank my friends and colleagues, especially my research group members in the Microtribodynamics laboratory, for their help and friendship. I would also like to thank Dr. Wilson Serem, the Associate Research Scientist at TAMU material characterization facility, for his valuable help and guidance in performing some of the experiments. Thanks also to department faculty and staff for making my time at Texas A&M University a great experience.

I would like to also thank the Hagler Institute for Advanced Study (HIAS) at Texas A&M University for partial funding of this study.

Last but not least, I warmest thanks to my parents for their unconditional love, constant support, and encouragement.

CONTRIBUTORS AND FUNDING SOURCES

Contributors

This work was supervised by a thesis committee consisting of the committee chair Prof. Andreas A. Polycarpou, and committee members Prof. M. Cynthia Hipwell, and Prof. Matt Pharr of the J. Mike Walker ’66 Department of Mechanical Engineering and Prof. Mohammad Naraghi of the Department of Aerospace Engineering.

The studies of 3D structures in Chapter 2 were conducted with the help of Dr. Jungkyu Lee, Dr. Yan Shi, Dr. Mengdi Han, and Dr. Xueju Wang. The studies of 3D structures in Chapter 3 were conducted with the help of Dr. Jungkyu Lee, Dr. Yan Shi, and Dr. Xueju Wang. The studies of 3D structures in Chapter 4 were conducted with the help of Dr. Mengdi Han. All other work conducted in the thesis was completed by the student independently.

Funding Sources

Partial funding of this study was provided by the Hagler Institute for Advanced Study (HIAS) at Texas A&M University. Kian Bashandeh acknowledges the support of HIAS through the HEEP graduate fellowship program.

TABLE OF CONTENTS

Page

ABSTRACT ii

ACKNOWLEDGEMENTS iv

CONTRIBUTORS AND FUNDING SOURCES v

TABLE OF CONTENTS vi

LIST OF FIGURES viii

LIST OF TABLES xi

1. INTRODUCTION AND LITERATURE REVIEW 1

1.1 Introduction 1
1.2 Assembly of 3D Structures Using Controlled Mechanical Buckling 2
1.3 Mechanical Performance of Kirigami Structures 3
1.4 Objectives and Outlines 4

2. THE EFFECT OF DEFECTS ON THE CYCLIC BEHAVIOR OF POLYMERIC 3D KIRIGAMI STRUCTURES 7

2.1 Introduction 8
2.2 Materials and Methods 9
2.3 Results and Discussion 12
2.3.1 Stiffening of the structures at 100% compression 12
2.3.2 Structures with Defects 14
2.3.3 Modeling using finite element analysis (FEA) 21
2.4. Summary 24
2.5 Supplementary movie legends 25

3. MECHANICS AND DEFORMATION OF SHAPE MEMORY POLYMER KIRIGAMI MICROSTRUCTURES 26

3.1 Introduction 27
3.2 Materials and Methods 29
3.2.1 Fabrication of the Structures 29
3.2.2 Modeling Using Finite Element Analysis (FEA) 32

3.3 Results and Discussion 34
3.3.1 Mechanical Cycling (15 Cycles) at RT 34
3.3.2 Shape Memory Property Characterization at Elevated Temperature 39
3.4 Summary 45
3.5 Supplementary movie legends 46

4. MECHANICAL CYCLING OF ENCAPSULATED 3D KIRIGAMI STRUCTURES 47

4.1 Introduction 47
4.2 Materials and methods 49
4.3 Results and discussion 52
4.4 Summary 60

5. CONCLUSION AND RECOMMENDATIONS FOR FUTURE WORK 62

5.1 Conclusions 62
5.2 Recommendations for Future Work 63

REFERENCES 65

LIST OF FIGURES

Page

Figure 1. (a) Conceptual illustration of fabrication of 3D Kirigami structures, (b) an example illustration of in-situ flat punch compression inside SEM. 3

Figure 2. Overview of research proposal. 5

Figure 3. (a) Schematic illustration of 2D design patterns and 3D Kirigami structures assembled by controlled buckling, and (b) corresponding SEM images of the fabricated structures (scale bar is 25 μm). 11

Figure 4. Structure without defect: (a) Load-displacement curves for 30 cycles of loading-unloading, compressed to 100 %, (b) Separated cycling curves for each set, and (c) SEM images taken before and after 30 cycles, including superimposed initial and deformed structure (scale bar is 25 μm). 14

Figure 5. (a) Table structure load-displacement curves for 30 cycles compressed to 100 %, (b) Separated cycling curves for each set, (c) SEM images taken before cycling and after each set of cycles (scale bar is 25 μm for the low magnification images and 5 μm for the high magnification images), and (d) Superimposed SEM images before the experiment and after the 30^{th} cycle (scale bar is 25 μm). 17

Figure 6. (a) Table structure load-displacement curves for 40 cycles at 100 %, (b) Separated cycling curves for each set, and (c) SEM images taken before and after 40^{th} cycles, including superimposed initial and deformed structure (scale bar is 25 μm). 19

Figure 7. Table structure load-displacement curves for cycling at 50 % compression (a) no defect [19], (b) pre-buckled leg defect, and (c) SEM images taken before cycling and after 50 cycles, including superimposed initial and deformed structure (scale bar is 25 μm). 21

Figure 8. The schematic illustration of 2D design patterns for Kirigami structures with different types of defect before compressive buckling 22

Figure 9. FEA results for single compression to 100% for the structures with and without defects. The dashed circle shows the site of defect in the structure. 23

Figure 10. Schematic illustration of the procedure to fabricate the 3D SMP Kirigami structures. 30

Figure 11. Schematic illustration of 2D precursors and their corresponding 3D buckled structures assembled by compressive buckling. 30

Figure 12. Optical images of three different 3D kirigami microstructures on elastomer substrate. The scale bars are 500 μm. 32

Figure 13. Load-displacement curves for cycling of structure 1 at (a) 20% compression, (b) 30% compression at different loading rates of 5, 10, and 25 μms^{-1}. Set 1 = cycles 1 - 5, Set 2 = cycles 6 - 10, Set 3= cycles 11 - 15. 36

Figure 14. Load-displacement curves for cycling of structure 2 at (a) 20% compression at different loading rates of 5, 10, and 25 μms^{-1}, (b) 30% compression at 5 μms^{-1}, with only one cycle shown since the structure broke, as shown in Figure 6(a). 37

Figure 15. Optical microscopy image (from the top) of (a) structure 2 and (b) structure 3 after 30% compression. The two broken legs are pointed with arrows. The scale bar is 500 μm. 38

Figure 16. Load-displacement curves for cycling of structure 3 at (a) 10% compression at different loading rates of 5, 10, and 25 μms^{-1}, (b) 20% compression at 5 μms^{-1}, with only one cycle shown since the structure broke, as shown in Figure 6(b). 39

Figure 17. SEM images and corresponding FEA (% maximum principal strains) for structures 1, 2, and 3 at different steps of the compression process. 42

Figure 18. Superimposed SEM images for structures 1, 2, and 3 before compression and after recovery (the dashed lines show the structure after recovery). 43

Figure 19. FEA results showing von Mises stress distributions (MPa) for compression of the structures at RT and high temperature of 72 °C (note that the scales are different for the stress contours). 44

Figure 20. FEA results showing maximum principal strain distribution (%) for compression of structures 1, 2, and 3 at RT and temperature of 72 °C. 44

Figure 21. Optical microscopy images of structures (a) without encapsulation, or plain structure, and structures encapsulated with (b) Dragon Skin, (c) Ecoflex, and (d) PDMS (the scale bar is 200 μm). 51

Figure 22. Load–displacement curves for cycling of Plain structure at (a) 10% compression, and (b) 20% compression. (c) the optical images of the structure showing the height of 250μm, and (d) change in the height of the structure before and after cycling. 53

Figure 23. Load–displacement curves for cycling of structure encapsulated with Dragon Skin at (a) 10% compression, and (b) 20% compression, and (c) the optical images of the structure at different positions. 54

Figure 24. Load–displacement curves for cycling of structure encapsulated with Ecoflex at (a) 10% compression, and (b) 20% compression, and (c) the optical images of the structure at different positions. 55

Figure 25. Load–displacement curves for cycling of structure encapsulated with PDMS at (a) 10% compression, and (b) 20% compression, and (c) the optical images of the structure at different positions. 56

Figure 26. (a, b) Variation of the device stiffness with number of cycles for 10% and 20% compression, respectively, and (c) variations of device load-bearing capacity for different encapsulation materials. 58

Figure 27. Load-displacement curves for cycling of structures encapsulated with (a) Ecoflex, and (b) PDMS. The calculated mechanical properties were obtained from the load-displacement curves: (c) maximum load-bearing and (d) stiffness at 20% compression. 60

LIST OF TABLES

Page

Table 1. SEM of structures with/without defects tested at 50 and 100% compression. ..12

Table 2. Utilized parameters for modeling of thermo-viscoelastic and shape memory behavior of the structures using a multibranch viscoelastic model. 34

Table 3. Calculated averaged stiffness values for structures at different compressions and loading rates. 35

1. INTRODUCTION AND LITERATURE REVIEW

1.1 Introduction

Biological structures are intrinsically based on hierarchical and three-dimensional (3D) designs with span of length scales from nano to macro scale [1]. Exploiting and mimicking the advantages with such 3D structures in biomaterials pave a design route for fabrication of humanmade devices with advanced capabilities and similar functionalities to biomaterials [2]. Hence, there is a growing interest in realizing these 3D structures with various shapes and scales in different applications such as electronics [3,4], biomedicine [5,6], mechanical and metamaterials [7,8], energy harvesters [9,10], microelectromechanical systems (MEMS) [11,12], and many other technologies.

Existing fabrication methods such as 3D printing, two-photon/multiphoton lithography, templated growth, and self-assembly have been employed to form the 3D structures, but each approach has certain limitations, which restricts the efficiency of production and device performance. These approaches can be utilized for a limited number of materials and are incompatible with lithographic techniques [1]. Therefore, alternative techniques based on strain-induced bending/folding have been suggested to overcome the drawbacks and limitations mentioned earlier [13,14]. Inspired by the ancient Japanese art of Kirigami (the art of cutting and folding), recent research reports on an established new method for fabrication of 3D structures based on compressive buckling of 2D precursors, which are already bonded to predefined locations on a prestretched elastomer substrate.

1.2 Assembly of 3D Structures Using Controlled Mechanical Buckling

The assembly of 3D structures by means of controlled mechanical buckling relies on transformation of 2D precursors to 3D shape by means of compressive forces induced by the release of prestrained substrate. This strain relief concept is inspired by the Japanese art of Kirigami, and therefore in this thesis, the structures are named "3D Kirigami structures".

Figure 1(a) depicts the schematic illustration of 2D to 3D transformation upon release of the prestrain in the elastomer substrate. Spin coating followed by photolithography and reactive ion etching forms the 2D precursors' layout. Transfer printing the 2D layout to a prestrained elastomer substrate with predefined bonding sites leads to strong covalent bonding at these sites. Release of the prestrain ($\varepsilon_x = \varepsilon_y = 0$) induces compressive forces, which creates out-of-plane deformation in the non-bonded regions of the precursors, thereby forming the desired 3D shapes. Unlike the other manufacturing techniques, this fabrication method is fast and capable of yielding a wide range of geometries, layouts, and combination of materials (e.g., polymers, metals, inorganic semiconductors, etc.) over a wide range of length scales (nanometers to meters), which implies the scalability of the method [1]. In addition, the functional materials such as piezoelectric membranes, shape memory polymers, or doped single-crystalline silicon can be integrated into the structures for the intended applications [15].

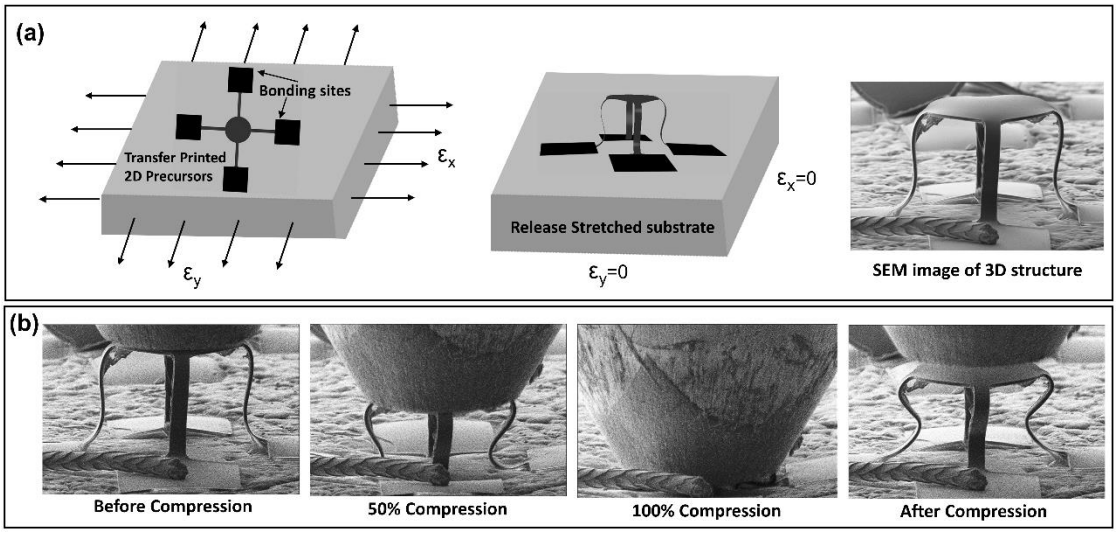

Figure 1. (a) Conceptual illustration of fabrication of 3D Kirigami structures, (b) an example illustration of in-situ flat punch compression inside SEM.

1.3 Mechanical Performance of Kirigami Structures

Integrating the 3D structures in applications such as flexible and stretchable electronics or 3D MEMS sensors requires a high level of durability and maintaining of performance against repeated deformations, which is imposed during operation by external stimuli. Therefore, the mechanical response of the fabricated 3D structures to the applied load needs to be investigated before exploiting them to the real application. Novel experimental techniques such as in-situ SEM flat punch compression can be used as a strong experimental tool for mechanical characterization of the structures. The advantage of performing the experiments inside the SEM is the ability to observe the deformation under the applied load and possible fracture event. In addition, one could also simultaneously measure the mechanical response (e.g., load-displacement) and observe the deformation. Thus, in this thesis, where applicable, the experiments were performed

inside SEM to investigate the deformation behavior of different fabricated 3D Kirigami structures. **Figure 1(b)** shows an example to illustrate the in-situ SEM experimental method. Before the experiment, the flat punch is brought to the proximity of the top membrane, and then the experiment begins by compressing the structures to different percentage of the height. For example, 50% compression denotes compressing to 50% of the structure's height.

1.4 Objectives and Outlines

A large number of studies have been performed to realize different classes of Kirigami-inspired 3D structures with different 3D layouts, materials, and sizes [1,16,17]. Nonetheless, little is known about the mechanics of these structures, and only a few studies have investigated the deformation behavior [15,18,19]. Therefore, this work is dedicated to studying the mechanics of various 3D Kirigami structures made of different materials such as SU8 epoxy, shape memory polymers, and polyimides, each intended for different applications. **Figure 2** illustrates an overview of the research ideas and the objectives that will be met throughout the thesis. 3D Kirigami structures were fabricated using compressive buckling method. The structures were made of different materials, namely SU8 epoxy, E44 shape memory epoxy, and polyimide (PI). The PI structures were encapsulated with different polymers to fabricate a more realistic type structure utilized in the applications. The mechanical response of assembled structures was studied through mechanical cyclic and single loading compression at room and elevated temperatures. Computational modeling was implemented for supporting the experimental findings and better understanding of deformation and fracture of the structures.

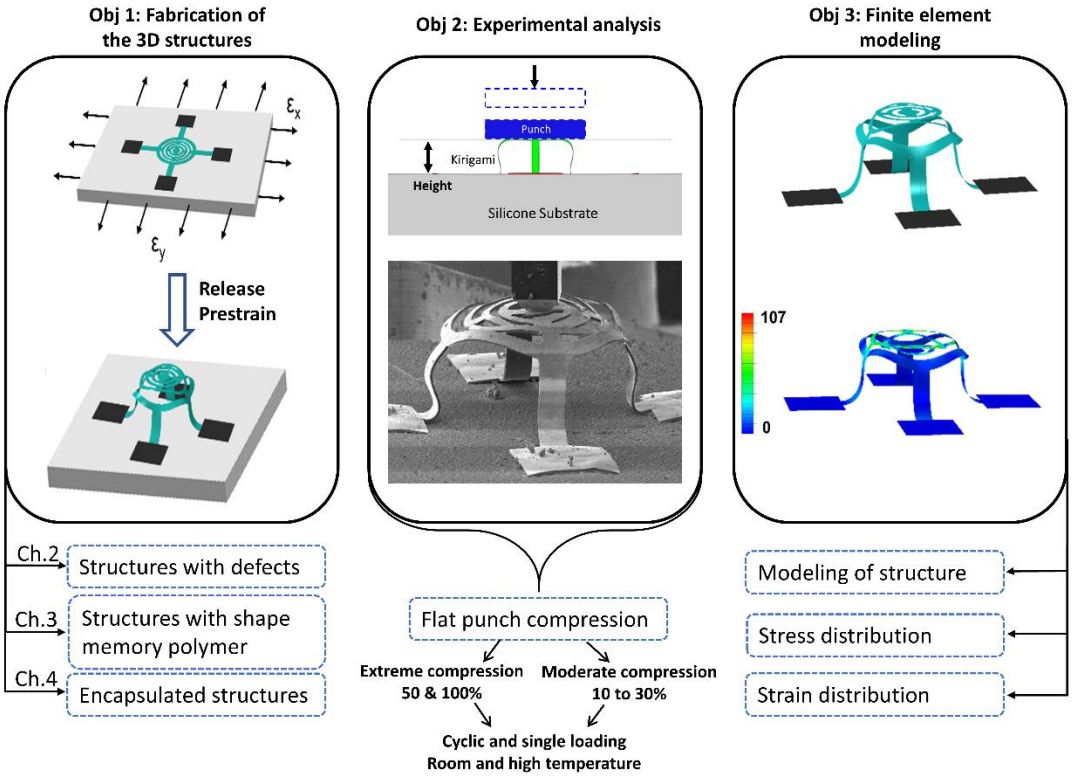

Figure 2. Overview of research proposal.

Chapter 2 discusses the fabrication of 3D SU8 Kirigami structures and investigates the role of different structural defects on mechanical cyclic behavior. Properties such as resilience, hysteresis loss, stability, and load-bearing capability were analyzed and compared with the structure without defect. The experiments were performed inside SEM using flat punch compression. The structures were compressed to 50 and 100% of the initial height. Chapter 3 presents the fabrication and deformation of 3D Kirigami-inspired structures made of shape memory polymer (SMP). Although a variety of 3D SMP structures with different geometrical and materials arrangements were fabricated already their mechanical response to applied load is still unknown. Therefore, in this Chapter, the

mechanics of these Kirigami structures were studied at room and elevated temperatures. In Chapter 4, the PI was used as the material for fabrication of the structures. In addition, piezoelectric monocrystalline Si-NM elements were integrated into the precursors, and thereafter the entire structures were encapsulated with a thin coating of different polymers.

The information presented in this thesis should be of great interest in understanding the mechanics of 3D polymer-based Kirigami-inspired structures. The work is expected to contribute to the current and future research on the development of flexible and stretchable electronics, biomedical devices as in tissue repair and vascular stents, as well as adaptive and deployable structures in aerospace engineering.

2. THE EFFECT OF DEFECTS ON THE CYCLIC BEHAVIOR OF POLYMERIC 3D KIRIGAMI STRUCTURES[1]

Recent advances in the assembly of three-dimensional (3D) structures driven by compressive buckling have provided an opportunity to exploit the capability in a broad range of engineering applications. These include microelectromechanical systems, energy storage, and wearable electronic devices. The occurrence of defects during fabrication and assembly, or during operation could impact the performance of the devices. Herein, we investigate the mechanical cycling of structures with different types of structural defects, including the presence of a pre-existing crack, structures with a thinner leg, and a pre-buckled leg. Studies of compressive cycling response of these microscale 3D polymer-based Kirigami architectures revealed stiffening behavior for both defective and non-defective structures. Structural densification, developed internal stress, and deformation of the elastomer substrate were the reasons for stiffening. Cyclic compression was performed to 50% and extreme condition of 100 % of the initial height using in-situ scanning electron microscopy. The structures were found to achieve stable hysteretic cycling with steady-state mechanical response after a number of cycles. The deformation behavior, the structure stability under cyclic loading, and the load-bearing capability were found to be dependent on the defect type, but they were not catastrophic.

---

[1]Reprinted with permission from "The effect of defects on the cyclic behavior of polymeric 3D kirigami structures" by Bashandeh K, Humood M, Lee J, Han M, Cui Y, Shi Y, Huang Y, Rogers JA, Polycarpou AA, Extreme Mechanics Letters. 2020, 18:100650. Copyright 2020 Elsevier.

2.1 Introduction

Three-dimensional (3D) architectures have emerged as a promising replacement of conventional two-dimensional (2D) structures, due to their application in nano/micro electromechanical systems (NEMS/MEMS) [12,20,21], biomedical devices [22,23], energy storage devices [24,25], stretchable and wearable electronics[26,27], robotics [21,28], and elsewhere [29–31]. With recent advances in fabrication techniques, such as strain-induced folding/bending and compressive buckling, inspired by the ancient art of origami/kirigami, various programmed configurations and scales of 3D structures, from sub-micron to macro-scales can be realized from 2D patterns [1,12]. In this work, the compressive forces created by releasing the prestrained elastomer transform the non-bonded regions of 2D precursors into the desired 3D Kirigami shapes [2].

The successful implementation of such 3D structures in practical applications requires a high level of efficiency and reliability. For example, the mechanical reliability of MEMS devices is a critical concern that must be considered from design to fabrication, and ultimately functionality [32,33]. The ideal situation for structures in applications such as 3D MEMS, sensors, or energy harvesting devices, is to sustain the external load and associated repeated deformation for extended periods of time. Factors such as geometry and thickness of the structure, the level and number of cyclic loading, and defect-induced degradation during fabrication process, could limit this lifetime and lead to unwanted malfunctioning of the devices.

In an earlier study, we investigated the mechanical resilience of different geometries of 3D kirigami structures under single compressive loading, and found a strong

geometric dependent mechanical behavior in terms of flexibility and elastic recovery [18]. Energy dissipation and durability of these structures under repeated compressive cyclic loading were also examined [19]. The structures demonstrated elastic behavior with minimal hysteresis by compressing to 50% of their height. At the extreme condition of cycling to 100% compression, the structures achieved stable hysteresis after few cycles and 94% elastic recovery.

Herein, we investigate the mechanical responses of 3D Kirigami-inspired structures with different types of defects. In any microfabrication process, the aim is always to increase the yield. However, sometimes defects are introduced in these structures at different steps of the process. Since buckling is a defect-dependent deformation, it is essential to investigate how these structures behave under compressive loading with the existence of such defects. 3D structures with defects were fabricated using a controlled compressive buckling approach and mechanically tested under cyclic compressive loading using in-situ scanning electron microscopy (SEM).

2.2 Materials and Methods

Fabrication of the 3D structures started with patterning of 2D precursors of epoxy (SU-8, 3 μm thickness) by spin coating and photolithography on a layer of silicon dioxide (SiO_2, 800 nm thickness), which was previously formed on a silicon wafer by thermal oxidation. The exposed regions of the SiO_2 layer were then removed by wet etching in diluted hydrofluoric acid (HF). Spin coating and photolithography were used again to form another layer of photoresist (AZ 5214, 4 μm thickness) on the non-bonded regions of the precursors. The remaining buried SiO_2 layer under the precursors was eliminated by

another HF wet etching process, to facilitate the transfer printing of the precursors from the Si wafer to another silicone elastomer substrate (Dragon Skin®, 600 μm thickness). A layer of titanium (5 nm thickness) and SiO_2 (50 nm thickness) were deposited on the precursors by electron beam evaporation to enhance the adhesion of the bonding regions of the precursors with the elastomer substrate.

The 2D patterns were then transfer printed from the Si wafer to a water-soluble polyvinyl alcohol (PVA) tape using a polydimethylsiloxane (PDMS) stamp. To form a strong bonding between the elastomer substrate and the precursors, the silicone elastomer and the precursors on the PVA tape were exposed to ultraviolet-induced ozone treatment, which formed a hydroxyl termination. The elastomer was then biaxially stretched to 75% prestrain with a mechanical stage. The PVA tape and the 2D precursors were then laminated on the stretched elastomer substrate and baked at 70 °C for 8 min to yield a strong bond between the substrate and the bonding regions of the precursors. Thereafter, the PVA tape and photoresist layer were removed using hot water and acetone, respectively. Releasing the prestrained elastomer substrate induced compressive forces which enabled the out-of-plane deformation of the non-bonded regions of the precursors, forming the desired 3D shapes. A schematic representation of the 2D patterns and their transformation to 3D structures upon releasing the elastomer is illustrated in **Figure 3,** for a table structure without defect and with a crack type defect. Each resulting nominal kirigami structure is made of 3 μm thickness SU-8, and a height of 60 μm.

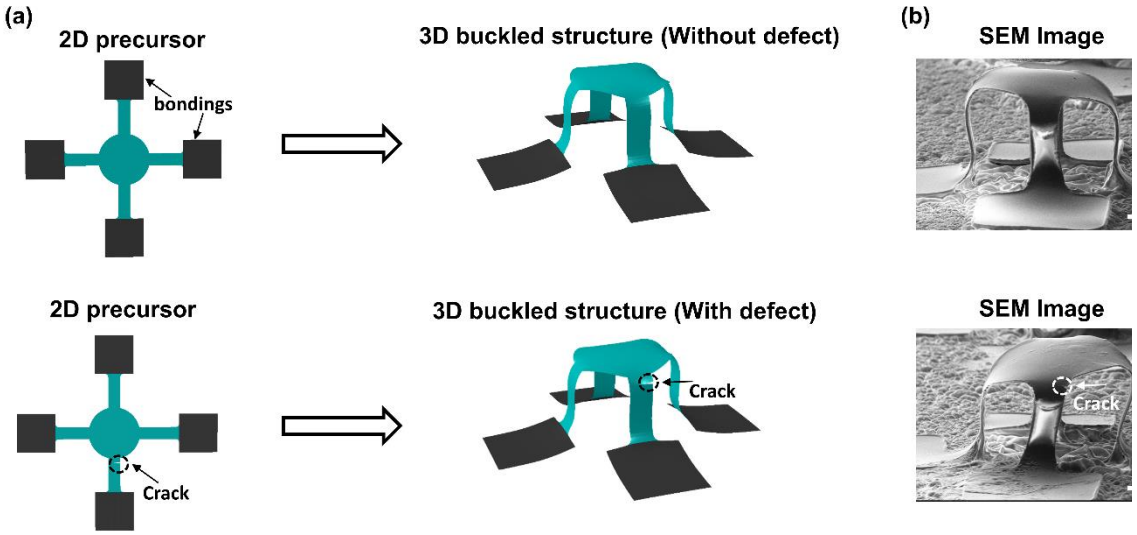

Figure 3. (a) Schematic illustration of 2D design patterns and 3D Kirigami structures assembled by controlled buckling, and (b) corresponding SEM images of the fabricated structures (scale bar is 25 μm).

The mechanical cyclic compression experiments were carried out on the structures with/without defects (shown in **Table 1**) using a commercial PI 88 SEM Picoindenter (Bruker) equipped with a diamond flat punch probe with a diameter of 100 μm. The samples were sputter-coated with 8 nm of Pt/Pd for better visualization inside the SEM. A displacement-controlled mode was used to compress the structures to 50% and 100% of their height.

Table 1. SEM of structures with/without defects tested at 50 and 100% compression.

Structures without defect		*Structures with defect*		
Table	Rotated table	Pre-existing crack	Thinner leg	Pre buckled leg
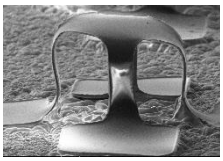	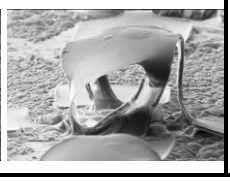	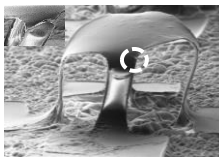	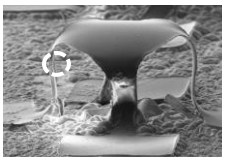	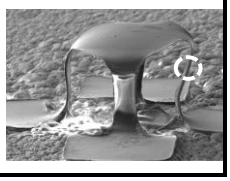

* The dashed circle shows the site of defect in each structure.

2.3 Results and Discussion

2.3.1 Stiffening of the structures at 100% compression

Figure 4(a, b) shows the load-displacement curves obtained by cycling of the rotated table structure to 100%. The curves in **Figure 4(b)** were divided for each set for clarity. Three sets of cycling experiments were carried out. Each set consisted of 10 cycles resulting in a total number of 30 cycles. 4 min was selected as the wait time after the complete unloading of the structure at the end of each set to allow for viscous relaxation of the structure/substrate. Note that the structure was fully unloaded only at the last cycle of each test set. The first cycle of each set, particularly set 1, demonstrated the largest hysteresis loop with the highest energy dissipation. This could be due to plastic deformation and initiation of buckling of the leg at the first cycle. Less energy was dissipated in subsequent cycles, indicating stabilization of the structure.

The load-bearing capacity increased with each set, as shown in **Figure 4(b)**. The curves showed three regions for the loading associated with Hookean-type deformation with a linear slope, a reduction in the slope due to small buckling, and an increase in the

slope due to stiffening of the structure. Similar behavior was observed for single compression of Kirigami structures [18]. The reasons behind the stiffening can be attributed to different mechanisms involved during the compression of the structure. Referring to the recorded **movie 1** in the supporting information, the densification of the structure with increase in compression forced the legs to ultimately touch the bonding pads and the substrate, wherein rapid increase in the force with small compression was initiated. According to [34], a slight curvature in a thin sheet can significantly increase the stiffness during bending, due to developed internal stresses. Here, the bonding pads behaved similar to a curved thin sheet subjected to bending at 100%. The role of substrate deformation became more dominant upon compression to 100%. The compression of the substrate indicated higher stiffness and load-bearing capability, compared to the structure [19].

The recorded **movie 1** shows that a combination of sliding, twisting, and slight bucking occurred with compression to 100%. The permanent buckling of the leg, and twisting of the structure can also be observed from the SEM images shown in **Figure 4(c)**, which were taken before the experiment and after the 30^{th} cycle. The buckling of the leg is shown with a dashed white circle in the SEM images. The superimposed image depicts a better visualization of the changes in the shape of the structure after the experiments. The dashed black line represents the initial structure before the experiment. From the superimposed image in **Figure 4(c)** three distinct deformation modes can be observed: (a) shifting to the right in the sliding direction, (b) slight reduction in the height due to buckling of the leg and plastic deformation, and (c) in-plane twisting of the structure.

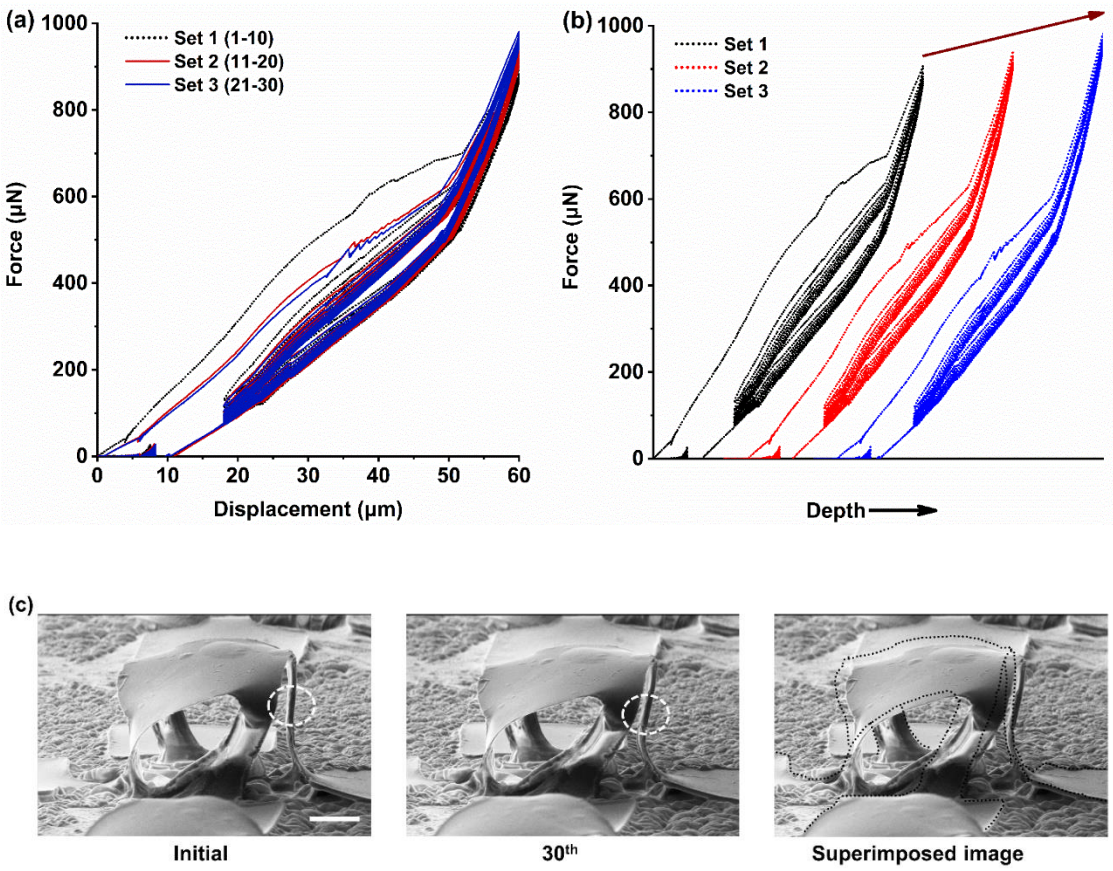

Figure 4. Structure without defect: (a) Load-displacement curves for 30 cycles of loading-unloading, compressed to 100 %, (b) Separated cycling curves for each set, and (c) SEM images taken before and after 30 cycles, including superimposed initial and deformed structure (scale bar is 25 μm).

2.3.2 Structures with Defects

2.3.2.1 Structure with Crack

The successful implementation of such 3D structures to practical applications such as 3D MEMS sensors requires high reliability and stability of the structures operating under cyclic mechanical loading. Such loading conditions can induce fatigue in the structure, which can ultimately lead to cracking and failure. In Ref. [19], we investigated

the mechanical response of a rotated table structure subjected to 200 cycles under extreme compression of 100%. The formation and growth of a microcrack were observed after the 100^{th} cycle. Herein, the structure had a pre-existing crack in one of the legs to capture a crack-type defect that could occur during the fabrication process.

Three sets of cyclic experiments with ten cycles at each set were conducted at 100% compression on a table structure with a small crack on its front leg, depicted with a white dashed circle in **Figure 5(c)**. **Figure 5(a, b)** show the load-displacement curves at each set. Initially, the structure demonstrated a Hookean response with linear elastic behavior followed by a large increase in the displacement with little increase in the load due to rapid buckling. Finally, a large increase in the load due to stiffening when the structure approached 100% compression. The first cycle showed the highest energy dissipation, while less energy was dissipated in the first cycle of the 2^{nd} and 3^{rd} sets. The structure achieved stable hysteresis and stabilized with increasing number of cycles. The structure became more robust and resistant to crack growth at subsequent sets.

A combination of sliding and buckling occurred during the compression to 100% (see the recorded **movie 2** for the first set). The buckling of the leg and permanent deformation of the structure is clearly discernible from the **movie 2**, as well as the SEM images shown in **Figure 5(c, d)**. **Figure 5(c)** shows the SEM images of the structure taken before the experiment and after each set of cycling tests. The higher magnification images show the growth of the crack with cyclic compression at each set. The comparison of the images after sets 2 and 3 (the 20^{th} and 30^{th} cycle) indicate negligible growth in the crack, compared to the 10^{th} cycle. The developed internal tensile stress on the leg resulted in the

crack growth. As seen in **movie 2**, the top portion of the leg is under tension with buckling of the leg inducing tensile stress at the crack site. The internal stresses decreased with number of cycles, which caused the crack growth to decelerate [35]. **Figure 5(d)** depicts the superimposed image before the experiment and after the 30^{th} cycle. The structure permanently deformed and tilted in the sliding direction, and the right leg experienced two-fold bending.

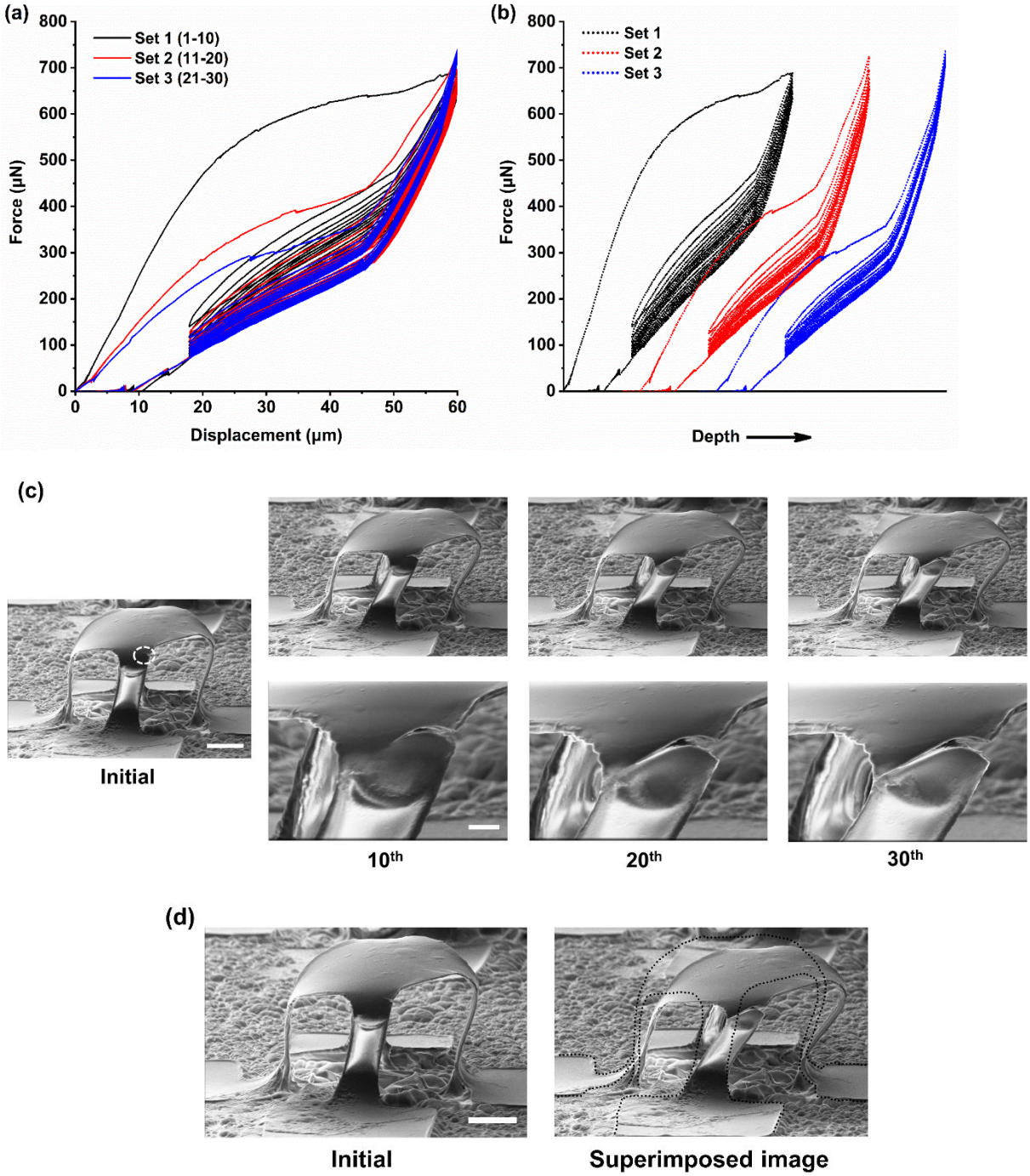

Figure 5. (a) Table structure load-displacement curves for 30 cycles compressed to 100 %, (b) Separated cycling curves for each set, (c) SEM images taken before cycling and after each set of cycles (scale bar is 25 μm for the low magnification images and 5 μm for the high magnification images), and (d) Superimposed SEM images before the experiment and after the 30th cycle (scale bar is 25 μm).

2.3.2.2 Structure with Thinner Leg

Numerical analysis of structures with different thicknesses showed the dependence of the mechanical response on the thickness of the structure [19]. Structures with lower thickness demonstrated a more compliant behavior with lower load-bearing capacity and stiffness. Here, the thickness effect is incorporated as a defect in the structure. The structure was compressed for 40 cycles at 100%. The respective load-displacement curves are depicted in **Figure 6(a, b)**. During the first cyclic loading, the structure followed a linear elastic behavior up to a threshold, where a sudden drop in the load occurred. Referring to the recorded **movie 3**, this sudden drop was accompanied by an instantaneous in-plane twisting and sliding of the structure as well as buckling of the right leg. The permanent twisting/buckling can also be observed in the SEM images depicted in **Figure 6(c)**. The right leg marked with a dashed white circle and the superimposed image before and after the experiments show the twisting/buckling in the legs. The sudden slip/twisting/buckling occurred due to the asymmetric supporting of the load by the legs. Subsequent cycling demonstrated a stable hysteresis with minimal degradation of the structure due to post-buckling/twisting stability. The load-bearing capability decreased after each set, particularly between 1^{st} and 2^{nd} sets.

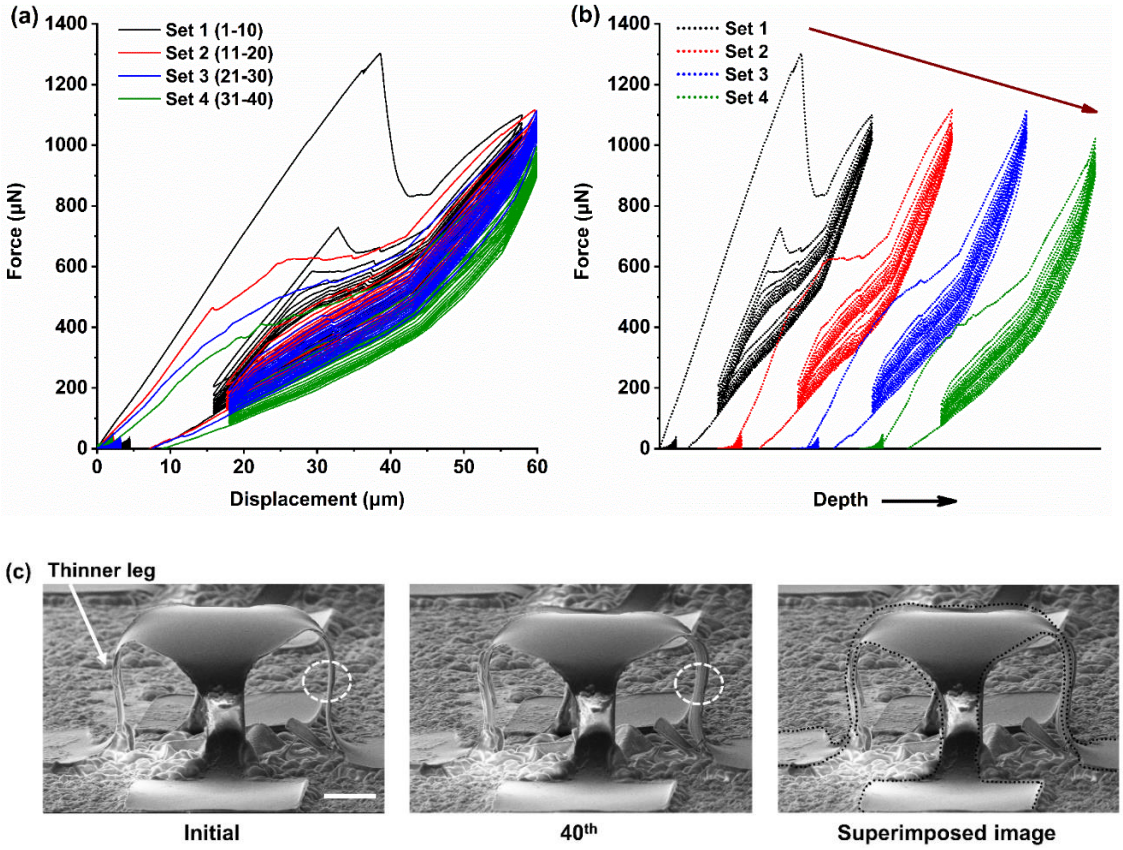

Figure 6. (a) Table structure load-displacement curves for 40 cycles at 100 %, (b) Separated cycling curves for each set, and (c) SEM images taken before and after 40th cycles, including superimposed initial and deformed structure (scale bar is 25 μm).

2.3.2.3 Structure with Pre-Buckled Leg

Figure 7(a) shows the cycling of a table structure without defect, which was carried out in an earlier study for 30 cycles at 50% compression [19]. The structure demonstrated a linear elastic behavior with minimal energy dissipation and stable hysteresis with complete recovery between each set. The defect considered in this section was introduced to the structure as buckling on one of the legs during the compressive buckling process. **Figure 7(b)** shows the cycling behavior of the structure at 50% for five

sets; each set consisted of 10 cycles. The maximum force dropped in the first cycle and then stabilized in subsequent cycles within each set. The load-bearing capability decreased between each set, as revealed by the downward shifting of the curves. In contrast to the structure without defect, the structure with defect dissipated higher energy and did not stabilize by the end of the cycling tests. The load-bearing capacity decreased by 37%, compared to the structure without defect. According to the recorded **movie 4**, the deformation was accompanied by large sliding due to the asymmetric support of the load by the legs. The buckled leg is marked in **Figure 7(c)** with a white dashed circle. The structure experienced a slight change in its shape in the sliding direction, as can be seen from the superimposed image.

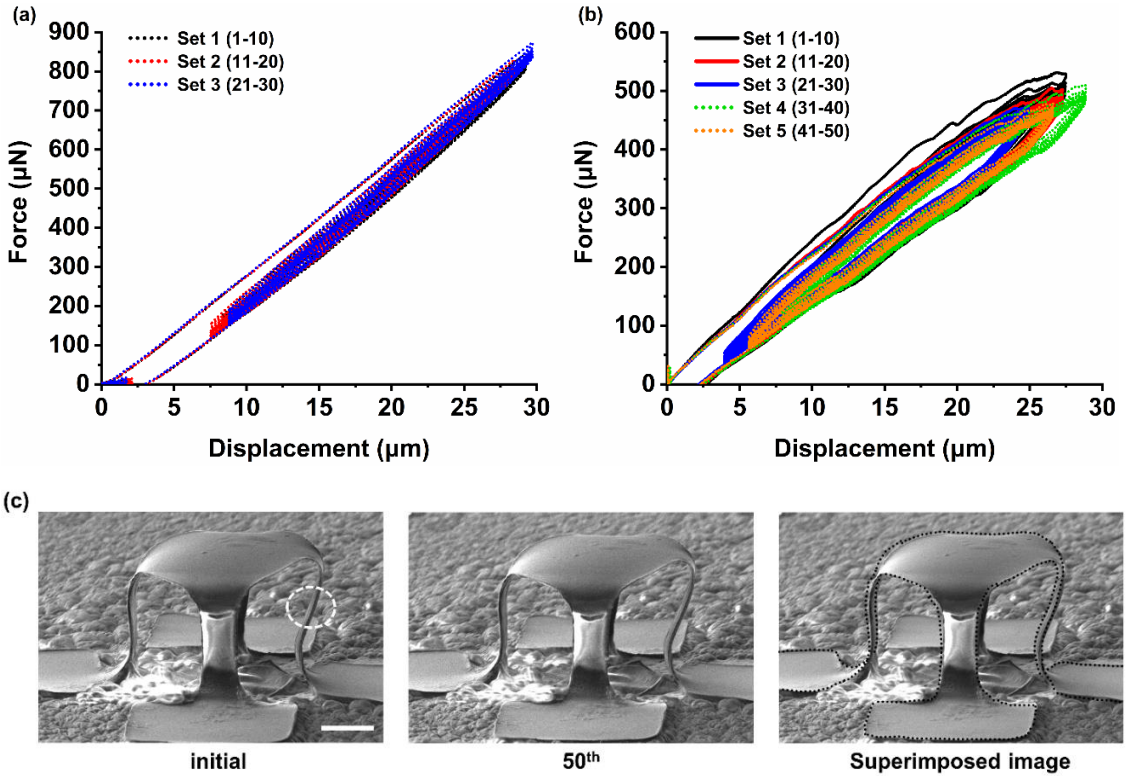

Figure 7. Table structure load-displacement curves for cycling at 50 % compression (a) no defect [19], (b) pre-buckled leg defect, and (c) SEM images taken before cycling and after 50 cycles, including superimposed initial and deformed structure (scale bar is 25 μm).

2.3.3 Modeling using finite element analysis (FEA)

3D FEA was conducted using the commercial software ABAQUS to simulate the structures with different types of defects. The goal was to investigate and compare the variations in configuration and stress/strain distributions upon compression to 100%. The structures and the elastomer substrate were simulated using four-node shell elements and eight-node 3D stress elements, respectively. The convergence of mesh size ensured computational accuracy. The SU8 Kirigami structures were assumed to be linear elastic with elastic modulus E and Poisson's ratio v of E_{SU8} = 4.02 GPa and v_{SU8} = 0.22,

respectively. Mooney Rivlin hyper-elastic model was used to model the elastomeric substrate with parameters C_{10} = 0.06757 MPa, C_{01} = 0.01689 MPa, and D_1 = 0.48 MPa^{-1}. The length for the legs of the structures were measured to be 55 µm, except the structure with pre-buckled leg defect, which was 65 µm. All legs had a thickness of 3 µm, except the structure with thinner leg defect, which had a thickness of 2.1 µm on its thinner leg. The 2D patterns the structures with each defect is shown in **Figure 8**.

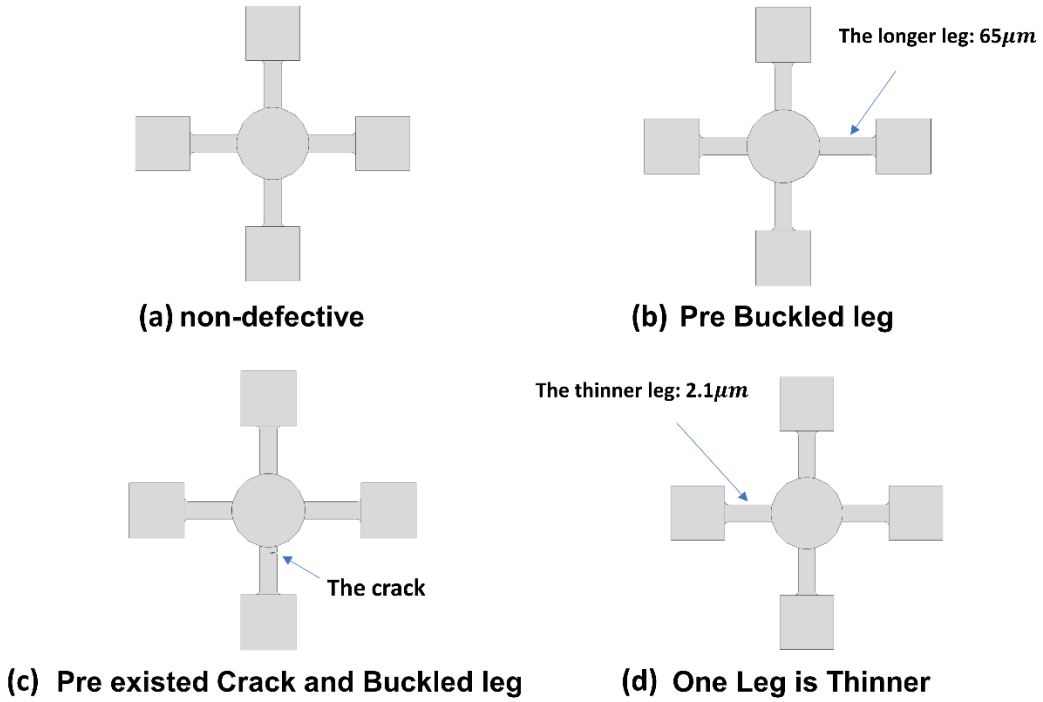

Figure 8. The schematic illustration of 2D design patterns for Kirigami structures with different types of defect before compressive buckling

Figure 9 shows the maximum principal strain and von Mises stress at 100% compression for the structure without defect and the structures with different types of

defects. For all structures except the structure with the pre-existing crack, the maximum strain and von Mises stress developed at the ribbon-membrane connections. The crack tip experienced the highest stress among the structures. The structure with thinner leg defect experienced the highest strain at the thinner leg with bending dominated deformation. The structure with pre-buckled leg showed similar strain behavior to non-defective structure, but higher stress at the top membrane-ribbon connection. All the structures exceeded the fracture threshold of SU8 (≈10%), leading to permanent plastic deformation in the legs.

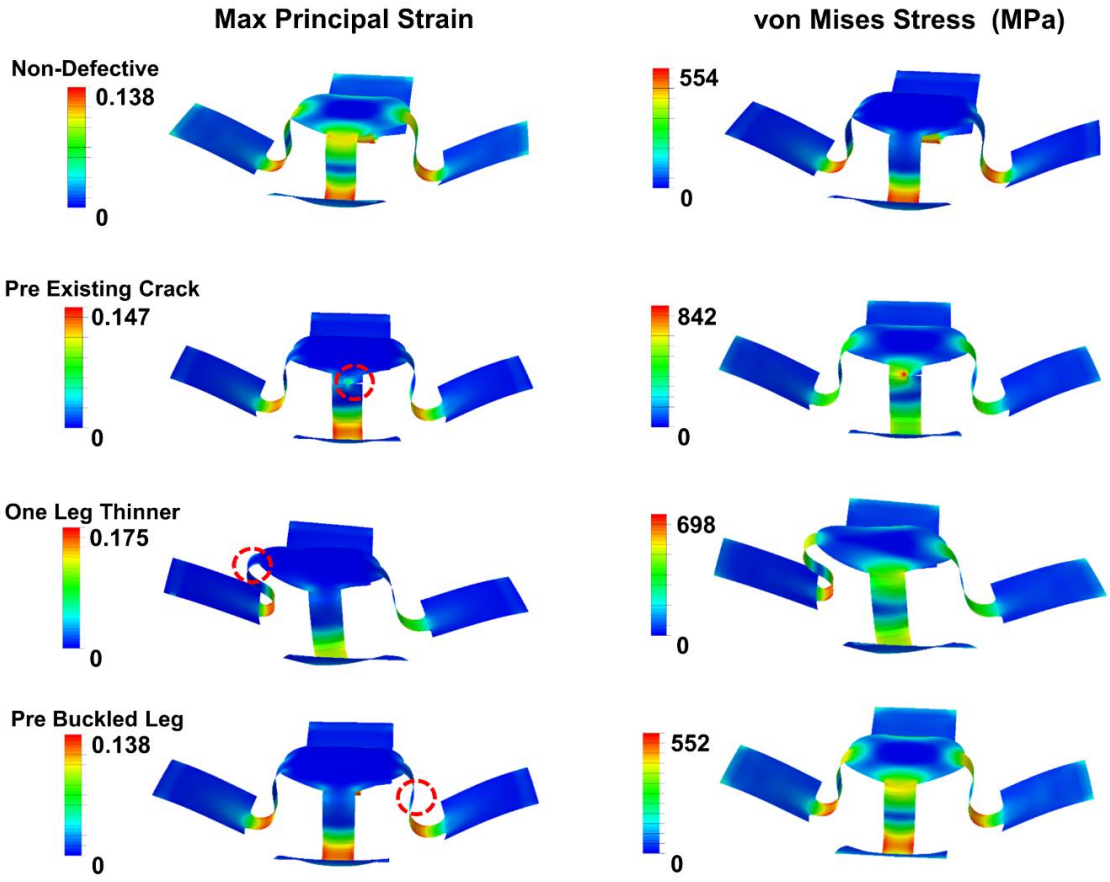

Figure 9. FEA results for single compression to 100% for the structures with and without defects. The dashed circle shows the site of defect in the structure.

2.4. Summary

Extreme mechanical cycling of 3D kirigami-inspired architectures with defects was performed using in-situ SEM flat punch compression at 50 and 100%. Three different types of structural defects, which could result during batch fabrication, were considered during the compressive buckling process. Apart from the possibility of occurrence of defects in the assembly process, these defects might also occur in practical applications during operation under extreme conditions. Therefore, it would be beneficial to know how the existence of defects would impact the mechanical response and durability against compressive cycling. Reduction in load-bearing capacity, energy dissipation, and deformation of the structures were found to be a function of the defect type. The crack type defect created a large plastic deformation in the sliding direction. The thinner leg type defect caused a sudden snap during the first cycle with a slight permanent twisting remaining after the experiments. The structures maintained stable hysteresis and achieved post-buckling stability after a few cycles, which is advantageous. Compared to the structure without defect, the pre-buckled leg in the structure induced non-instability in the load-displacement response with higher energy dissipation and decreased load-bearing capacity by 37%. The degree of plastic deformation was found to be a function of defect type. The existence of crack in one of the legs caused the largest plastic deformation. FEA results showed the dependency of stress/strain distribution and deformation on the defect type. The internally developed stress and the deformation of the substrate were the mechanisms behind stiffening, once compressed to 100%. It is worth noting that despite

the defect type, all structures ultimately achieved stable hysteresis with steady-state mechanical behavior, which is advantageous in practical applications.

2.5 Supplementary movie legends

Movie 1: Mechanical cycling of rotated table structure to 100% compression

Movie 2: Mechanical cycling of table structure with pre-existing crack to 100% compression

Movie 3: Mechanical cycling of table structure with thinner leg to 100% compression

Movie 4: Mechanical cycling of table structure with pre buckled leg to 50% compression

3. MECHANICS AND DEFORMATION OF SHAPE MEMORY POLYMER KIRIGAMI MICROSTRUCTURES[2]

The assembly of three dimensional (3D) structures through compressive buckling of 2D precursors can serve as a promising and robust tool to realize different classes of advanced materials in a broad range of applications with complex geometries and a span of length scales from sub-micron to macro scales. In this Chapter, a shape memory polymer (SMP) material was used as the precursor to form different configurations of 3D kirigami microstructures. 3D SMP structures can serve in a wide range of applications, such as biomedical and aerospace, which require a level of robustness and compliance. To this end, the mechanical response of assembled 3D buckled Kirigami structures were investigated through mechanical cyclic and single loading compression at room and elevated temperatures, respectively. The experiments at room temperature were performed to examine the mechanical resilience and stability of the structures upon repeated loading. The load-bearing capacity, resiliency, and stability under deformation were shown to be largely affected by their structural shape. In-situ scanning electron microscopy experiments at elevated temperatures demonstrated the outstanding shape memory behavior by full recovery to their original shape, without any structural damage or fracture.

---

[2] Reprinted with permission from "Mechanics and deformation of shape memory polymer kirigami microstructures" by Bashandeh K, Lee J, Wu Q, Li Y, Wang X, Shi Y, Guo X, Huang Y, Rogers JA, Polycarpou AA., Extreme Mechanics Letters. 2020, 10:100831. Copyright 2020 Elsevier.

Computational modeling supports the experimental findings and contributes to the understanding of deformation and fracture of the structures.

3.1 Introduction

Multiscale and three dimensional (3D) structures of biological materials with multifunctional properties have been utilized as a design route in many research studies to prepare bioinspired manmade materials and devices, with similar multifunctionality and integrity to biomaterials [36,37]. Such 3D structures with various shapes, configurations, and scales have been realized in applications, such as electronic systems [38–40], biomedical devices [41–43], energy storage [44,45], metamaterials [46,47], functional scaffolds for tissue engineering [48], and others [49,50]. Different fabrication techniques, including 3D printing [51], two-photon/multiphoton lithography [52,53], and strain-induced bending/folding [54] have been developed to form various 3D structures. Each technique has its limitations and constraints, such as material compatibility and accessible feature sizes and geometries [50,55].

Of these techniques, compressive buckling can serve as a strong tool in the assembly of 3D structures with different materials, geometries, and length scales. In this technique, the non-bonded regions of the 2D precursors on a prestrained elastomer substrate transform into a deterministically controlled 3D structure in a reversible manner through compressive forces induced upon the release of the prestrained elastomer [56]. Such structures are referred to as kirigami microstructures. Maintaining the 3D design shape upon the removal of prestrain requires the structure to stay on the assembly elastomer substrate. However, there are practical applications that require operating in a

condition that is not compatible with elastomer substrates, such as elevated temperatures, as in templates for materials growth, or applications which demand a freestanding structure in isolated forms, as in micro-robotics [48]. The freestanding 3D structure can be realized through shape fixation and memory effect using shape memory polymer (SMP) [48,57]. The implementation of 3D SMP-based structures provides the ability to recover from severe deformation and also enables programmable shape changes.

Although different 3D SMP structures have been fabricated, their mechanical response to applied load, and their reversibility is unknown. Past experimental investigations were confined to qualitative methods and not direct mechanical measurements [57,58]. The deformation and mechanical cycling of various configurations of 3D polymer-based kirigami structures were investigated using in-situ compression inside a scanning electron microscope (SEM) [18,59]. Herein, we perform in-situ cyclic compression of 3D SMP structures using an indenter equipped with a flat punch probe. Load-displacement responses, including cyclic loading were measured in-situ at room temperature (RT, 23 °C). Also, in-situ compression experiments inside a SEM were performed to directly observe the shape recovery of the structures after the removal of the stress, at elevated temperature. The experiments were initiated with heating the structures above their glass transition temperature (T_g) by 15 °C, followed by compressing the structures to 30% of their initial height. The structures fully recovered to their initial state upon reheating.

3.2 Materials and Methods

3.2.1 Fabrication of the Structures

Figure 10 illustrates a schematic representation of the fabrication process. Fabrication of the 3D SMP structures started with spin coating a thin layer of poly(4-styrenesulfonic acid) as a water-soluble sacrificial layer on a silicon wafer. Spin casting formed the 2D precursors of the SMP, composed of epoxy monomer E44 and curing agent poly(propylene glycol) bis(2-aminopropyl ether) (Jeffamine D-230) mixed with a mass ratio of 44:23. The samples were cured in a furnace for 1 hour at 110 °C. A lithographically patterned thin metal layer composed of 10 nm chromium (Cr) and 50 nm gold (Au) served as a hard mask for oxygen plasma etching of the SMP. Transfer of the 2D precursors from the silicon wafer to a water-soluble polyvinyl alcohol tape (PVA, 3M Co.) required the removal of the previously formed underlying sacrificial layer on the silicon wafer, which was accomplished by immersion in water. To define the bonding locations, a thin layer of titanium (Ti, 5 nm thick) followed by a thin layer of silicon dioxide (SiO_2, 50 nm thick) were deposited on selective locations of the precursors by using a flexible shadow mask (75 μm thick polyimide film). Before transfer printing the precursors to the stretched silicone elastomer substrate (Dragon Skin; Smooth-On, Easton, PA), the precursors on the PVA tape and the stretched substrate were exposed to ultraviolet ozone treatment to promote the bonding strength by inducing hydroxyl termination. Releasing the prestrained elastomer substrate after dissolving the PVA tape in water induced compressive forces on the 2D shape memory precursors, which enabled the out of plane deformation of the non-bonded regions of the precursors and thus forming the desired 3D kirigami structures.

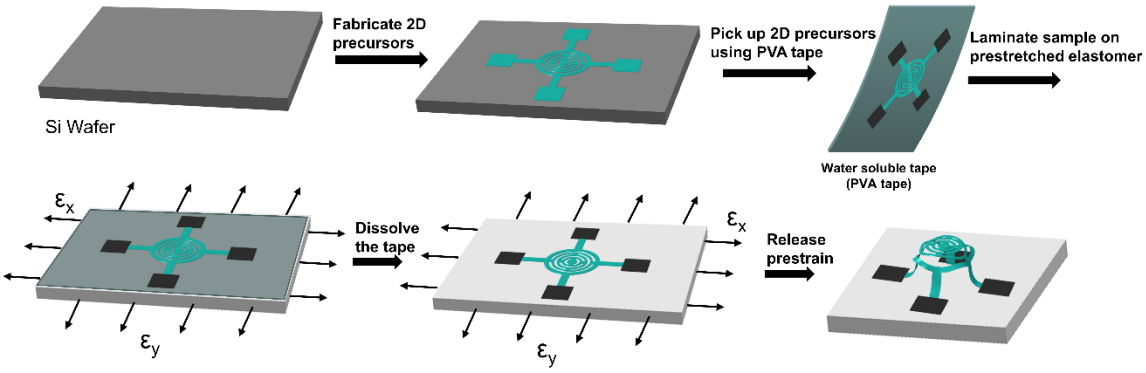

Figure 10. Schematic illustration of the procedure to fabricate the 3D SMP Kirigami structures.

A schematic representation of the 2D design patterns used in this work, and their corresponding 3D Kirigami structures upon release are shown in **Figure 11**.

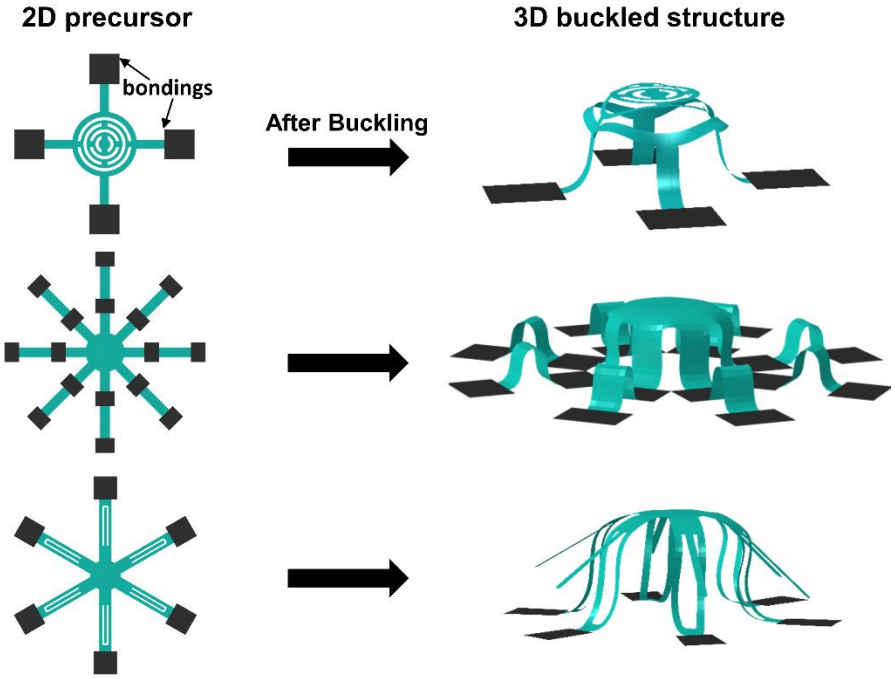

Figure 11. Schematic illustration of 2D precursors and their corresponding 3D buckled structures assembled by compressive buckling.

Figure 12 shows optical microscopy images of the three fabricated structures bonded on the substrate. The height of the structures was measured from the side view of the optical images, and found to be 510 μm, 260 μm, and 505 μm for structures 1, 2, and 3, respectively. All structures are supported with vertical legs but with different design, height, and number of legs. The structures were initially cyclically compressed to 20 and 30% of their initial height using an instrumented nanoindenter (TI 980, Bruker) equipped with a flat punch probe. Subsequently, structures 2 and 3 were respectively compressed to 20 and 10%, due to breakage and fracture of the structures at higher compression values at RT. Three loading rates of 5, 10, and 25 μms^{-1} were selected to study the load rate sensitivity. The experiments at elevated temperature were performed using in-situ SEM compression with a PI 88 SEM PicoIndenter (Bruker), equipped with a flat punch probe (100 x 100 μm^2 square). All structures were compressed to 30% for one loading-unloading cycle.

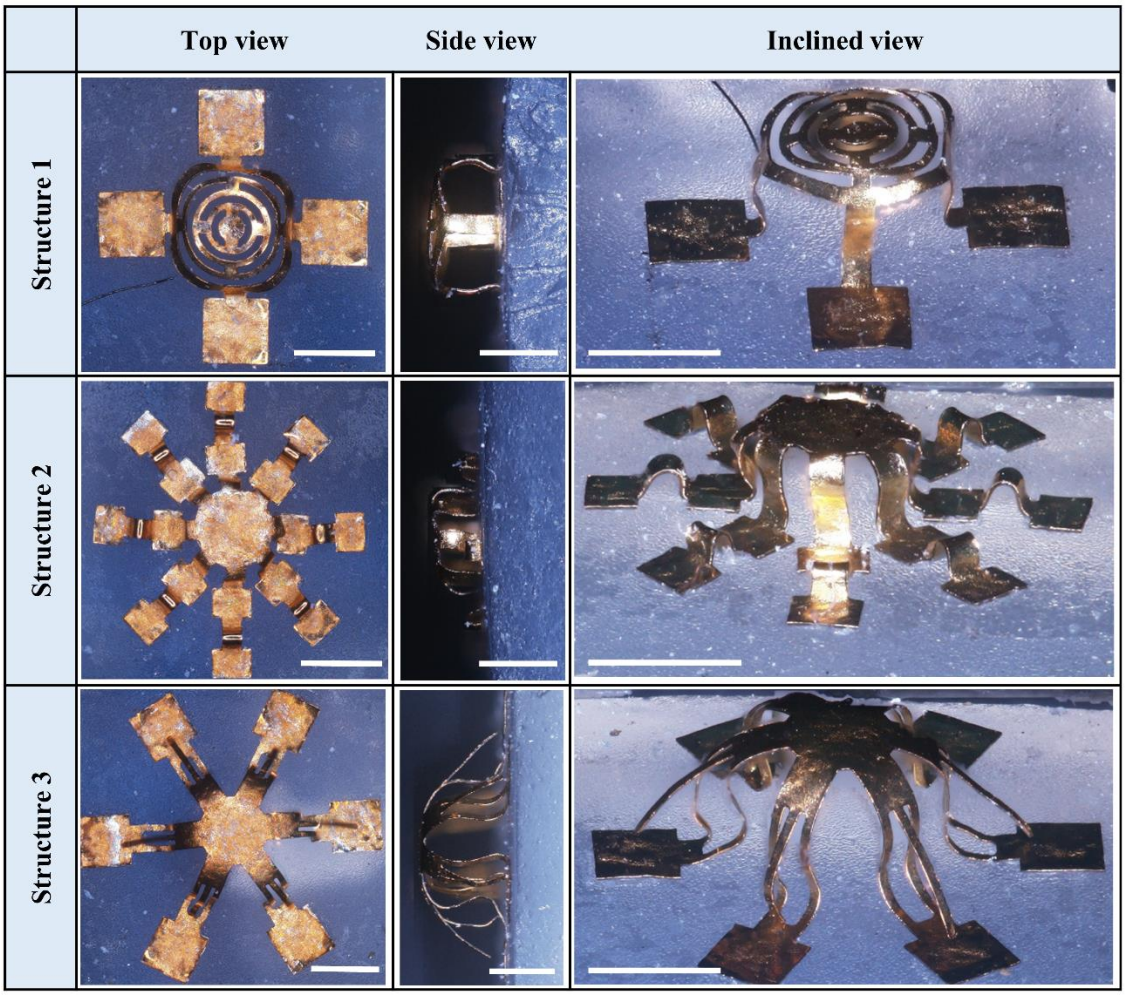

Figure 12. Optical images of three different 3D kirigami microstructures on elastomer substrate. The scale bars are 500 μm.

3.2.2 Modeling Using Finite Element Analysis (FEA)

Modeling was carried out through 3D FEA using the commercial software ABAQUS. The goal was to capture the 2D to 3D transformation through mechanically guided assembly and compare the stress/strain distribution upon compression at room and elevated temperatures. The silicone elastomer substrate (2 mm in thickness) and the precursors (10 μm in thickness) were modeled using eight-node 3D solid elements and

four-node shell elements, respectively. Refined meshes were used to ensure computational accuracy. The elastic modulus and Poisson's ratio values of the elastomer substrate were taken to be E = 166 kPa and ν = 0.49. To simulate the experiments, the prestrain was modeled to be 70% for structure 1, and 50% for structures 2 and 3. The shape memory material can be identified as a thermo-rheologically simple polymer whose thermo-viscoelastic behaviors can be described by a multi-branch rheological model [60]. In this model one equilibrium branch and several thermoviscoelastic nonequilibrium branches are arranged in parallel. Maxwell elements are used in the nonequilibrium branches to represent the stress relaxation behavior of the material [26]. The parameters for equilibrium and nonequilibrium branches are provided in **Table 2**.

Table 2. Utilized parameters for modeling of thermo-viscoelastic and shape memory behavior of the structures using a multibranch viscoelastic model.

Branch	$E^{non}(Pa)$	$\tau^{R}(s)$	**Branch**	$E^{non}(Pa)$	$\tau^{R}(s)$
1	3.725E08	3.000E-11	15	3.550E08	1.392E01
2	3.000E08	6.410E-10	16	2.800E08	2.655E02
3	3.300E08	8.210E-09	17	3.525E08	8.548E00
4	3.675E08	8.840E-08	18	2.047E08	7.588E01
5	4.150E08	8.210E-07	19	1.317E08	2.187E02
6	4.725E08	6.780E-06	20	3.120E07	1.961E03
7	5.200E08	4.840E-05	21	7.008E07	6.390E02
8	6.275E08	3.000E-04	22	4.281E06	8.055E03
9	4.450E08	1.500E-03	23	1.208E07	3.000E03
10	3.600E08	4.870E-03	24	2.994E06	1.280E05
11	3.775E08	1.418E-01	25	3.258E06	3.000E04
12	4.075E08	4.536E-01	26	4.567E02	5.420E05
13	4.050E08	1.500E00	27	6.342E06	3.000E06
14	3.775E08	4.729E00			
$E_s^{eq}(Pa)$	$E_{elas}(Pa)$	AF_c/k	$T_{ref}(°C)$	C_1	C_2
1.000E07	1.000E06	-2.000E04	45.000	17.400	60.350

3.3 Results and Discussion

3.3.1 Mechanical Cycling (15 Cycles) at RT

Figure 13(a, b) shows the load-displacement curves for cycling of structure 1 at 20 and 30% compression. The structure was consecutively compressed 15 times, and each 5 cycles is termed a set. The curves show two linear regions corresponding to compression of the top rings with linear elastic deformation, followed by a slight buckling in the legs of the structure. The first cycle showed different behavior with a higher hysteresis loop,

due to plastic deformation of the structure [59]. The slight plastic deformation is revealed by residual deformation upon removal of the load. The structure maintained minimal and stable hysteresis by increasing the number of cycles. The hysteresis, recovery, and energy dissipation remained the same between each test set. Compressing to 30% of the structure's height showed similar cyclic behavior but with higher load-bearing capacity and lower stiffness. According to **Table 3**, compressing the structure to 30% reduced the stiffness by 12%, compared to 20% compression. The increase of loading rate to 25 μms^{-1} slightly increased the stiffness by 4% at 20% compression. The structure achieved less hysteresis and stability with increase of the loading rate to 25 μms^{-1}.

Table 3. Calculated averaged stiffness values for structures at different compressions and loading rates.

#	Loading rate (µm/s)	Stiffness (N/m)	Loading rate (µm/s)	Stiffness (N/m)	Loading rate (µm/s)	Stiffness (N/m)
Structure 1 (20%)	**5**	9.01	**10**	9.18	**25**	9.35
Structure 1 (30%)		7.92		7.89		7.93
Structure 2 (20%)		234.06		239.21		234.51
Structure 3 (10%)		63.66		64.66		66.19

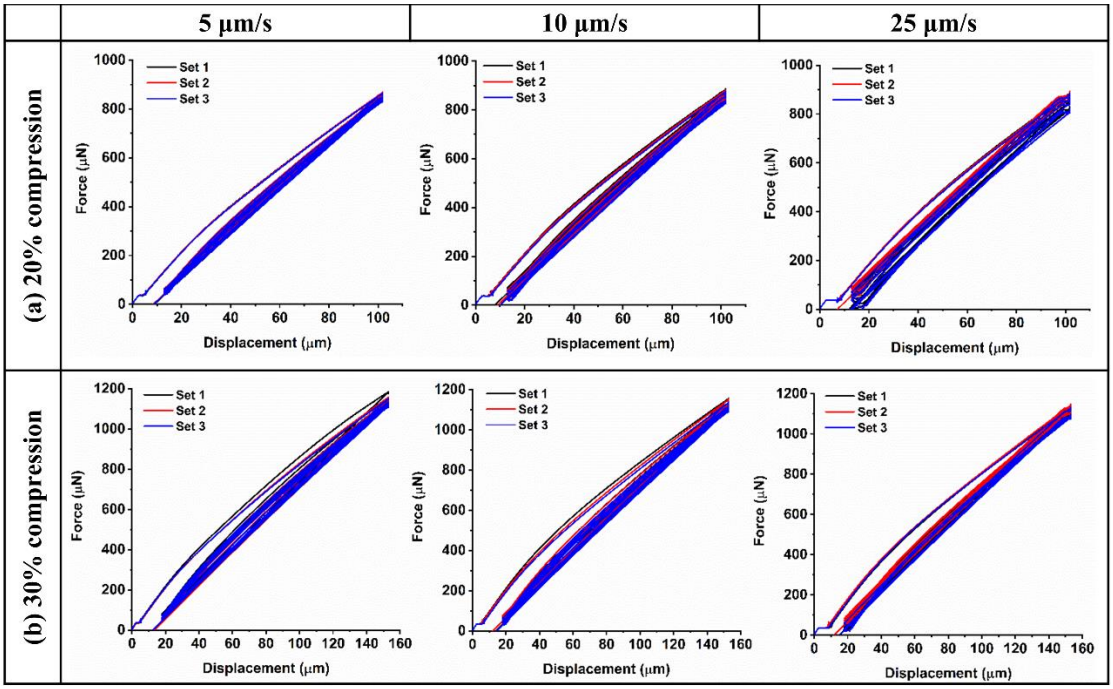

Figure 13. Load-displacement curves for cycling of structure 1 at (a) 20% compression, (b) 30% compression at different loading rates of 5, 10, and 25 μms^{-1}. Set 1 = cycles 1 - 5, Set 2 = cycles 6 - 10, Set 3= cycles 11 - 15.

Structure 2 was compressed at the same conditions as structure 1. The load-displacement curves are depicted in **Figure 14(a, b)** showing linear elastic deformation at all cycles. Similar to structure 1, the first cycle showed the highest hysteresis, and then exhibited minimal and stable hysteresis. The load-bearing capacity increased significantly compared to structure 1. The stiffness remained nearly unchanged at different loading rates (see **Table 3**). However, the stability reduced by increasing the loading rate to 10 and 25 μms^{-1}. While the structure could support the load up to 20% compression, cycling to 30% revealed a different behavior; namely, the structure could not support the load and broke at 70 µm displacement, which is captured by a sudden drop in the load-displacement

curve. The optical microscopy of the broken sample is shown in **Figure 15(a),** indicating the breakage of two legs from the top membrane.

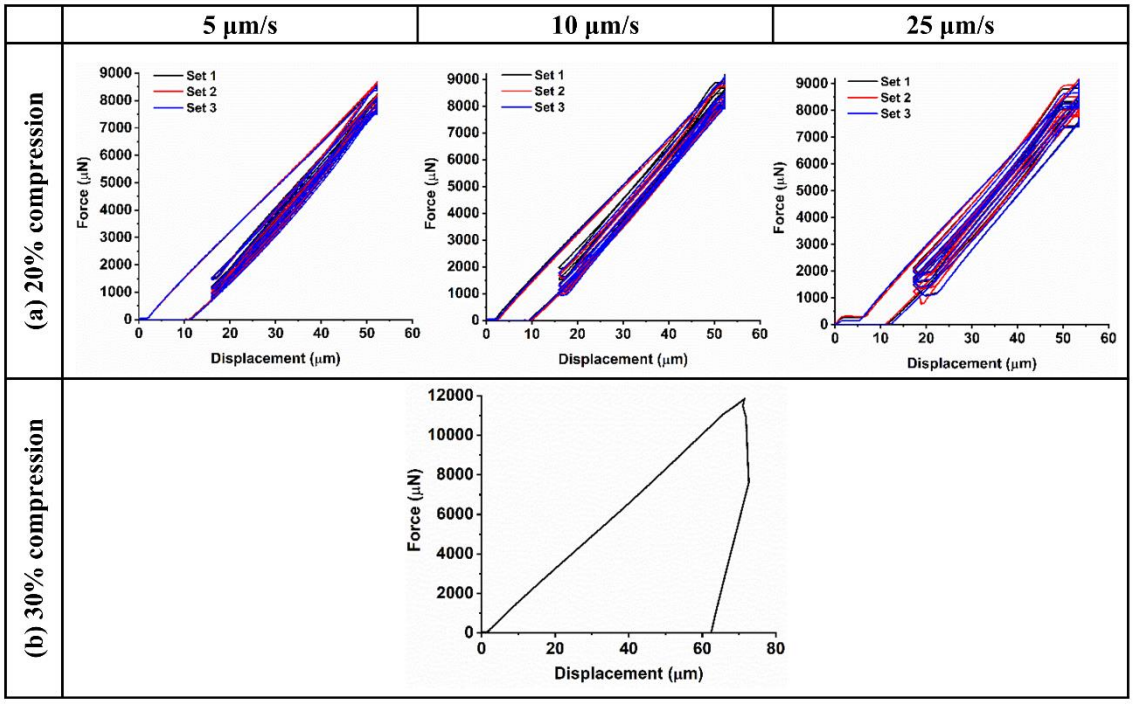

Figure 14. Load-displacement curves for cycling of structure 2 at (a) 20% compression at different loading rates of 5, 10, and 25 μms^{-1}, (b) 30% compression at 5 μms^{-1}, with only one cycle shown since the structure broke, as shown in Figure 6(a).

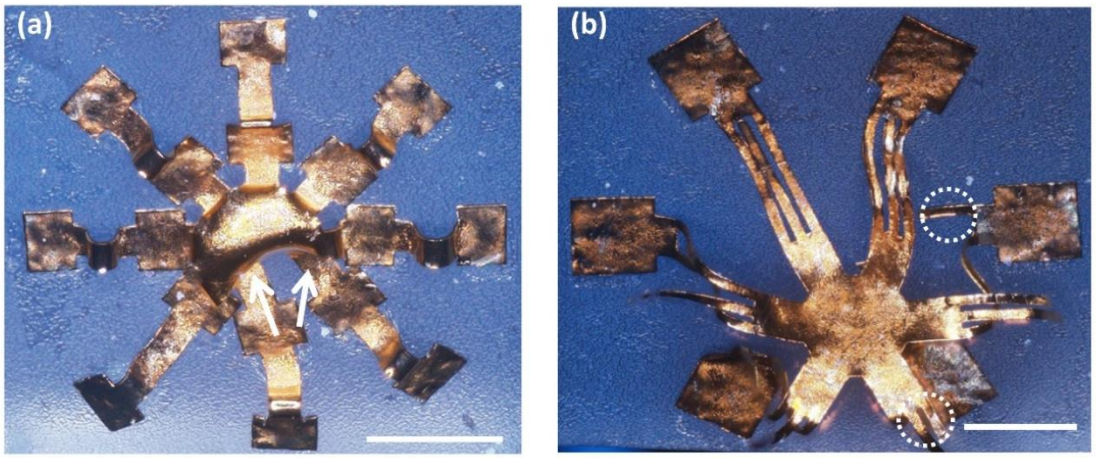

Figure 15. Optical microscopy image (from the top) of (a) structure 2 and (b) structure 3 after 30% compression. The two broken legs are pointed with arrows. The scale bar is 500 µm.

Figure 16(a, b) shows the cycling of structure 3 at 10 and 20% compression. Note that since the structure could not support the load at 20%, compression was reduced to 10% of the height. The deformation was dominated by linear elastic behavior at 10% compression. Unlike the other structures, the first cycle did not show significant difference in the hysteresis loss, compared to the subsequent cycles, especially at the lower loading rate. The structure fully recovered to the initial state upon the removal of the load (at 10% compression). The experiments at higher loading rates revealed dependency of hysteresis and stability of the structure to the frequency of cycling tests. The hysteresis remained stable and without change between each set at the lowest loading rate. However, increasing the loading rate to 10 μms^{-1} imposed a slight shift to the load-displacement curve but with similar hysteresis. At the maximum loading rate, due to unstable behavior, the experiments stopped after set 2. From **Table 3**, the increase of loading rate to 25 μms^{-1} slightly increased the stiffness by 4%. The structure could not support the load when

compressed to 20% and broke at 90 µm displacement. **Figure 15(b)** shows an image of the structure after the experiment, indicating folding and breakage of the legs. The third structure showed the least hysteresis and medium load bearing capacity among the three structures.

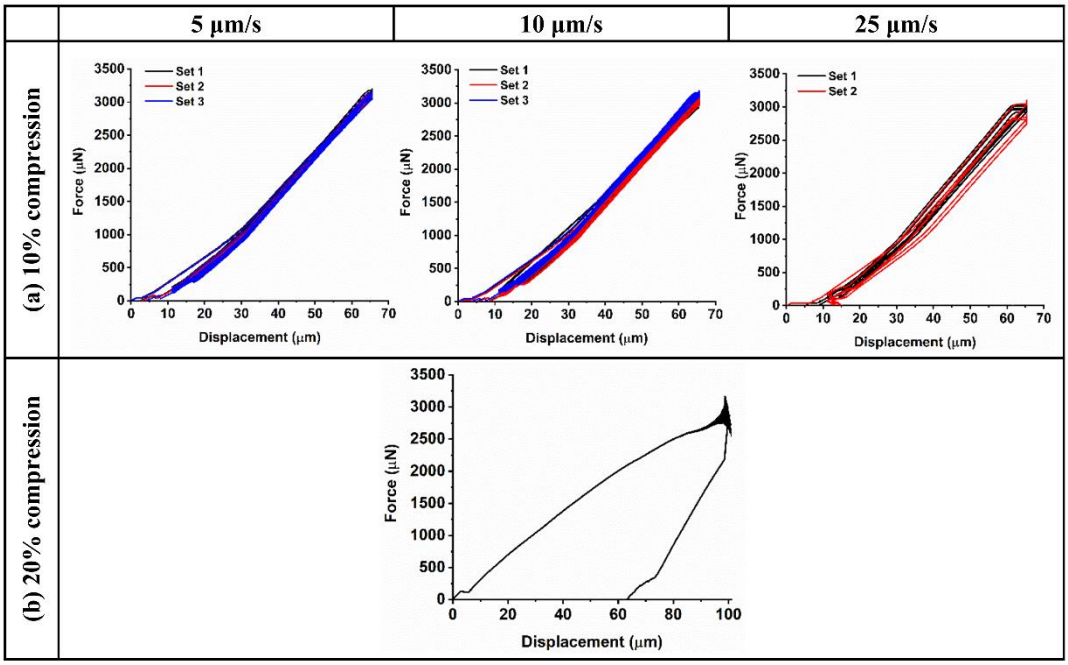

Figure 16. Load-displacement curves for cycling of structure 3 at (a) 10% compression at different loading rates of 5, 10, and 25 µms^{-1}, (b) 20% compression at 5 µms^{-1}, with only one cycle shown since the structure broke, as shown in Figure 6(b).

3.3.2 Shape Memory Property Characterization at Elevated Temperature

The capability of SMPs to recover from a fixed deformed shape to their original shape was investigated through in-situ SEM mechanical compression. Exposing the structures to external stimuli such as heat, light, and pH triggers the shape memorization in the material [61]. A second similar exposure after deformation recovers the structure to

the original shape. In this work, heating was used as the external stimulus. The experimental process followed three steps: I) heating the structures above the glass transition temperature (where T_g = 57 ℃), which triggered high mobility and flexibility in the chains. Upon transition, the structures become soft and the storage modulus changes from 3 GPa to 10 MPa [57]. II) Followed heating, the structure was compressed by 30% using a flat punch probe and cooled down to RT, while it was under the applied load. During cooling the chains locked in place and the structures stayed in the deformed shape. III) Upon removal of the load, the structure was heated again with the same initial heating rate, in which case the structure recovered to its original shape.

Figure 17 shows a direct comparison of the experimental results and FEA simulations, and the latter gives the strain distribution. The SEM images were taken from all three structures at different steps of the experimental process: 1) image after heating the structures above T_g to 72 ℃, 2) image of the structures under 30% compression after cooling down to RT and removal of the flat punch probe from the structures, and 3) image after reheating to 72 ℃ showing the recovered structures. The images at step 2 show the deformed structures indicating different deformation mechanisms.

Supplementary **movies 5-7** show the in-situ deformation mechanisms upon compression and the recovery after releasing of the load for the three structures. Note that the movies are sped up at different rates during the cycle of heating-cooling-heating. Examining **movie 5** (structure 1), the majority of the deformation occurred in the inner rings of the structure with slight buckling on the legs. The recovery followed the same behavior starting from the inner rings and the legs. For structure 2, the majority of the load

was supported by the legs causing more resistance to compression, which was also observed by the high load-bearing capacity of the structure in the RT experiments. As seen in **movie 5** (structure 2), the support of the load by the legs caused deflection on the top membrane leaving a concave shape after cooling. Such mechanism is responsible for failure of the sample during the RT experiments. Furthermore, the FEA results show the strain concentration at the top membrane, in agreement with the experiments. From **Figure 15(a)**, the failure at RT was initiated at the top membrane, where the maximum pressure and deflection took place. Similar to structure 1, the recovery started from the membrane and the legs.

A combination of sliding and bending deformation occurred for structure 3 and became larger at higher compression. From **movie 7** (structure 3), the legs on the site of the sliding direction experienced twofold bending, while the rest of the legs deformed under onefold bending. As seen in **Figure 15(b)**, the failure of the structure at the leg sites during the RT experiments is due to the asymmetrical support of the load, with more severe deformation of the legs in the sliding direction. In addition, the corresponding FEA results indicate similar location where the maximum strain concentration occurred. Recovery followed the same path as loading, starting from recovery of the legs in the sliding direction. Despite the RT experiments, where some of the structures failed, the activation of shape memory effect resulted in full recovery of all three structures. From the superimposed images in **Figure 18**, all the structures demonstrated 100% recovery without any structural damages and fracture, indicating their outstanding shape memory behavior.

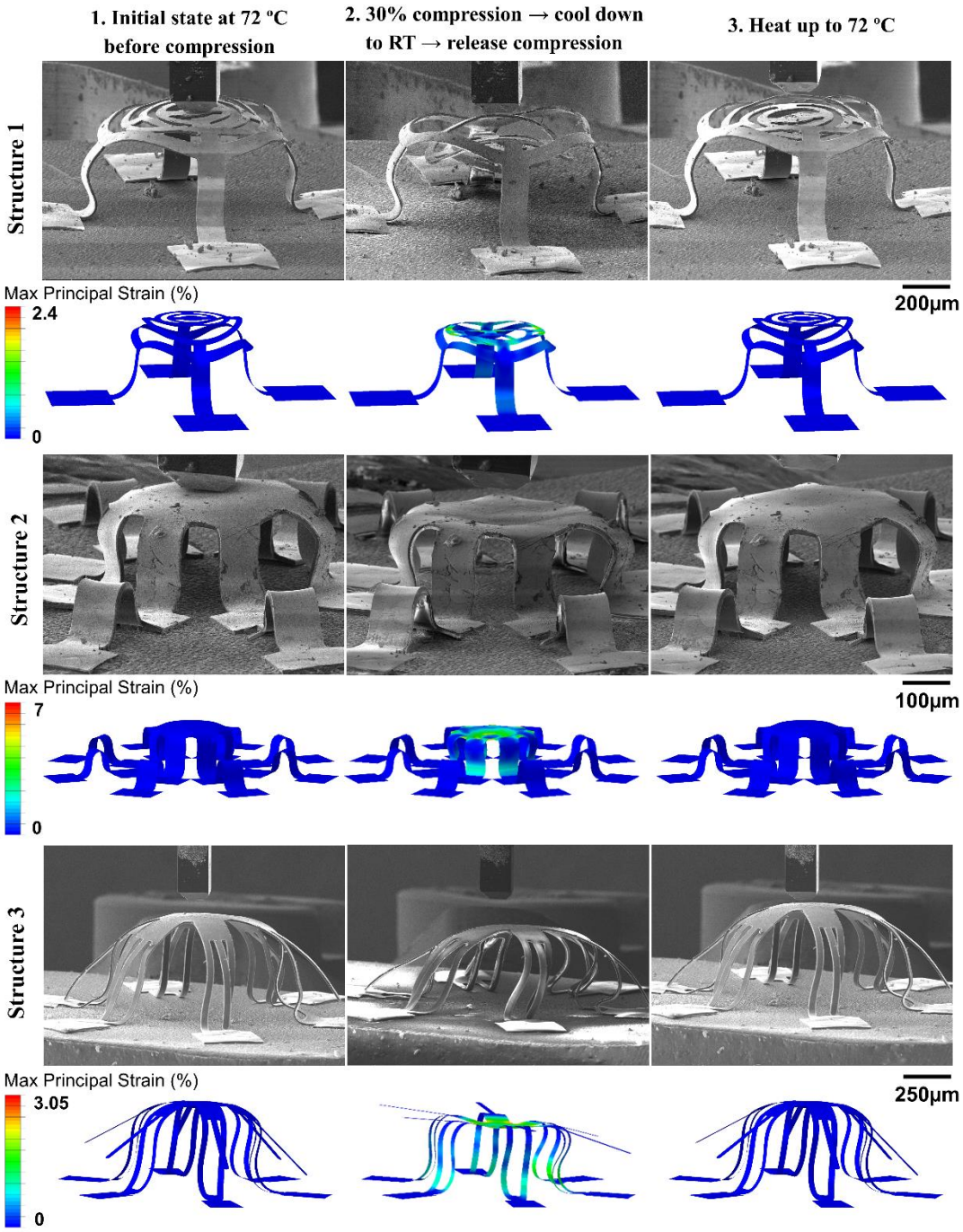

Figure 17. SEM images and corresponding FEA (% maximum principal strains) for structures 1, 2, and 3 at different steps of the compression process.

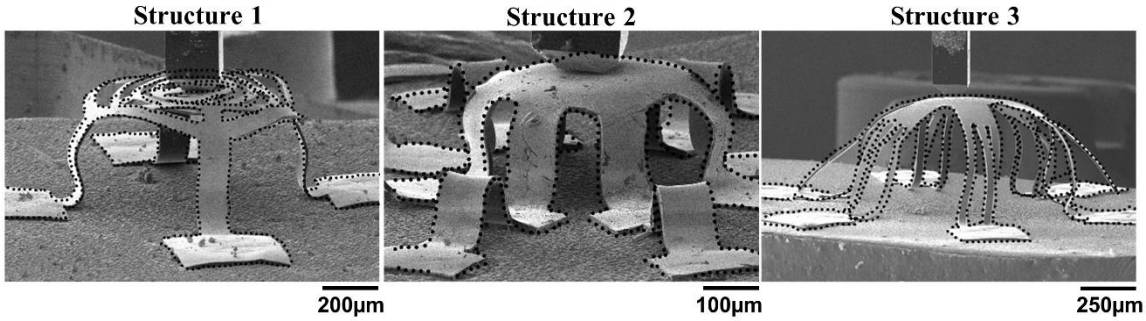

Figure 18. Superimposed SEM images for structures 1, 2, and 3 before compression and after recovery (the dashed lines show the structure after recovery).

FEA simulations were carried out to compare the stress/strain distributions at room and elevated temperatures. **Figure 19** and **Figure 20** show the contours of von Mises stress and maximum principal strain, respectively, upon compression to 30%. The compressions at RT have almost the same strain values compared to high temperature, as the structures compressed under similar compression. The von Mises stress increased significantly upon compression at RT as the modulus is higher at RT, compared to elevated temperature. Structure 2 experienced the highest stress among the three structures, and which located at the top membrane and membrane-ribbon connections. Note that this is the same location where fracture of the structure occurred at RT experiments (see **Figure 15(a)**). Structures 1 and 3 showed nearly similar maximum stress values, but with different distribution. The maximum stress was located at the membrane-ribbon connections of structure 3, where bending deformation took place and fracture occurred (**Figure 15(b)**).

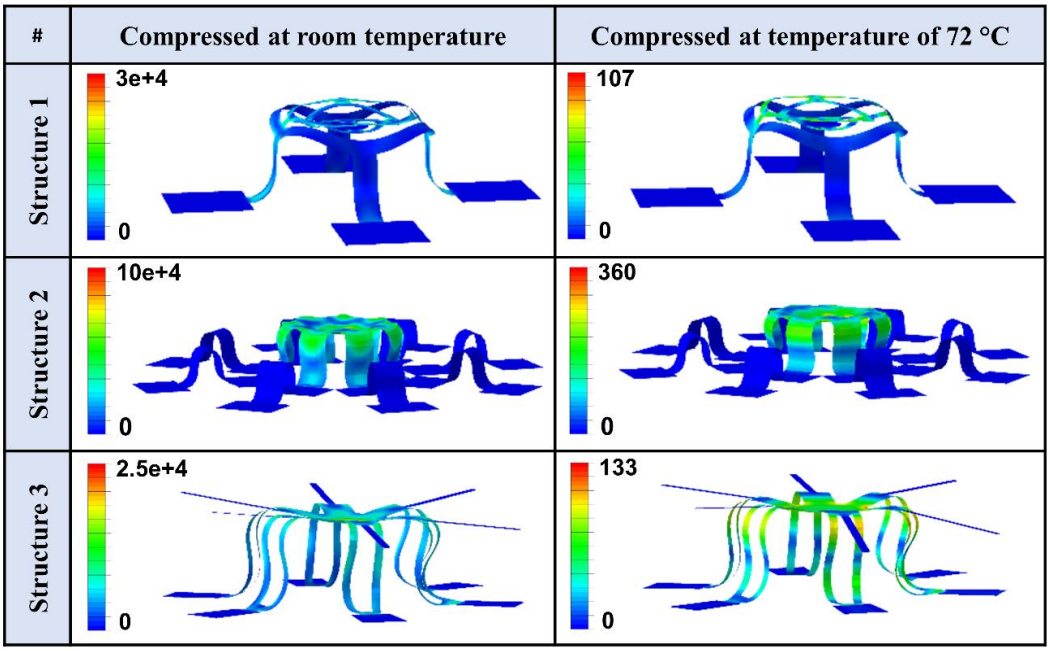

Figure 19. FEA results showing von Mises stress distributions (MPa) for compression of the structures at RT and high temperature of 72 °C (note that the scales are different for the stress contours).

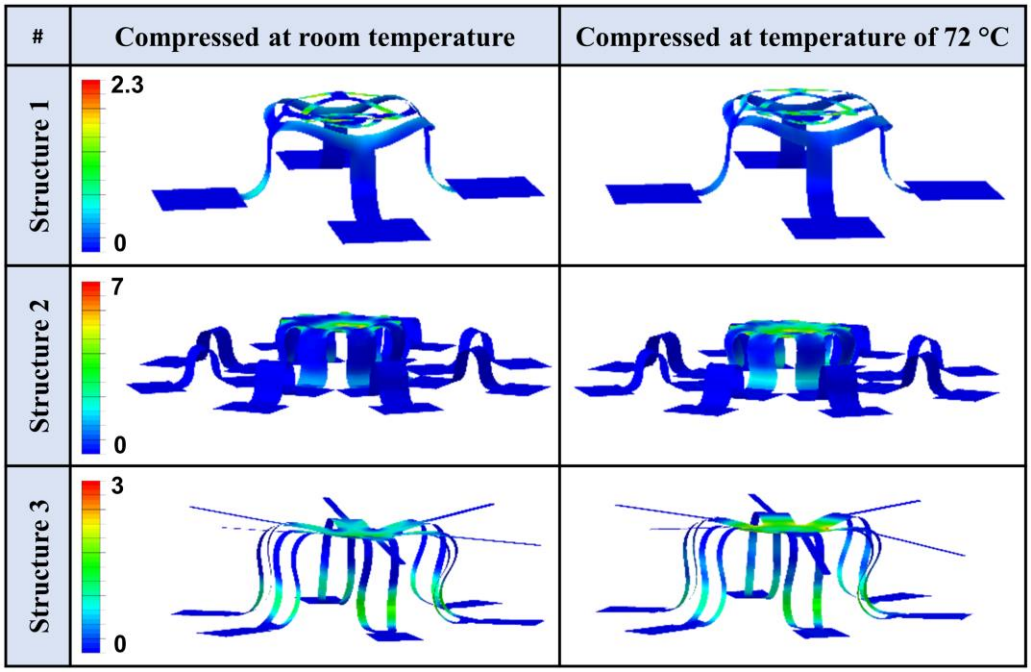

Figure 20. FEA results showing maximum principal strain distribution (%) for compression of structures 1, 2, and 3 at RT and temperature of 72 °C.

Flexible, robust, and shape-programmable 3D SMP kirigami-inspired structures reported here are promising for different applications, including biomedical devices for tissue repair and vascular stents [62], as well as adaptive and deployable structures in aerospace engineering [63]. In addition, the mechanics-deterministic nature of the 3D buckling technique allows freedom to design and fabricate 3D structures of well-controlled geometries in advanced materials, including combination of SMPs with functional electronics. Although epoxy SMPs are used in this work, the fabrication and characterization techniques developed herein are applicable to SMPs with a wide range of glass transition temperatures (20 - 300 ℃) for various applications.

3.4 Summary

3D kirigami microstructures were fabricated with different geometrical configurations from epoxy shape memory polymer, using compressive buckling. The mechanical response of the structures was measured at room and elevated temperatures, under cyclic and single compressive loading, respectively. The goal was to evaluate the resilience and stability of the structures upon compression from 20% to 30% of their initial height, and examine and compare their behavior with experiments at elevated temperature with shape memory effect.

The experiments at RT revealed strong dependency of mechanical performance upon deformation (e.g., resilience, load bearing capacity, stiffness, and energy dissipation) to the initial configuration of the structures. The simplest quad-leg structure 1 showed the lowest load bearing capacity and stiffness, but the highest resilience compared to the other more complex structures. The most complex octa-leg 16 bonding sites structure 2, showed

the highest load bearing capacity and stiffness but lower stability and higher hysteresis, compared to structure 1. Hexa-double leg structure 3 showed the lowest hysteresis and medium load bearing capacity and stiffness, but the least resilience upon compression, as the sample fractured beyond 10% compression. The in-situ SEM compression experiments at elevated temperature (above glass transition) demonstrated the shape memory effect in the structures. All structures fully recovered to their initial state after experiments at 30% compression. Unlike the experiments at RT, no structural fracture was observed after the experiments. Modeling using FEA indicated that the fracture of structures 2 and 3 at RT experiments could be attributed to their structural design, von Mises stress, and their distribution. Shape memory is an effective way to enhance the performance of these flexible kirigami microstructures upon loading.

3.5 Supplementary movie legends

Movie 5: Deformation and recovery of structure 1

Movie 6: Deformation and recovery of structure 2

Movie 7: Deformation and recovery of structure 3

4. MECHANICAL CYCLING OF ENCAPSULATED 3D KIRIGAMI STRUCTURES

3D Kirigami-inspired microsensors were fabricated using compressive bucking method. The structure was integrated with piezoresistive elements and encapsulated with polymers with different stiffness. The mechanical response of assembled 3D buckled structures were investigated through mechanical cyclic at 10 and 20% compression. The goal was to evaluate the stability and durability of the device against multiple cycles of loading, frequency of applied external stimuli, viscoelastic effect, and load-bearing capability of the encapsulant materials. To this end, mechanical cycling from 30 to 100 cycles was performed with loading rates varying from 5 to 15 μm/s. Additional faster experiments were performed with a frequency of 1 Hz to simulate the frequency of human walking for simulating the conditions in the intended application.

4.1 Introduction

The advantages of 3D nature biological systems and structures have motivated researchers to mimic their capabilities in humanmade devices in applications such as biomedical prosthetics [64], electronic skin [65,66], and health monitoring [67,68]. An example of such 3D structure in the human body is the sensory receptors, which are responsible for the detection of external stimuli. The incorporation of such 3D designs to piezoelectric devices such as sensors and actuators provided valuable advances in the device capabilities, which would be difficult to achieve with 2D systems [69]. An example is the improved frequency tunability and bandwidth of 3D MEMS compared to 2D structures [70].

Different techniques have been developed for the fabrication of 3D structures such as 3D printing [71], two-photon/multiphoton lithography [72], and thin-film folding and wrinkling [73]. Among these fabrication methods, compressive buckling is proved to be of particular interest due to its unique advantages such as the accessible feature size, scale, and material [1]. The compressive buckling technique relies on the 2D to 3D geometrical transformation of the precursors, which are selectively bonded to a prestretched elastomer substrate. Releasing the prestrain in the substrate induced compressive force that pops up the 2D precursor into a programmable 3D shape.

In this Chapter, the mechanical performance of 3D tactile sensors is investigated using an experimental approach by flat punch compression. The 3D sensors were fabricated using compressive bucking method, and the Table-like shape was selected for the structural design of the sensor. Piezoelectric monocrystalline silicon nanomembranes (Si-NMs) were integrated into the body of the structures at selective locations and the whole layout was encapsulated with a thin layer of polymers with different stiffnesses to complete the fabrication process. The stiffness is an important aspect in the design of 3D devices intended for mechanical sensing and harvesting. For example, ultralow stiffness is of interest for systems with low-frequency response and in soft biology [45].

The durability of the device against many cycles of loading, the frequency of applied external stimuli, the viscoelastic effect and the load-bearing capability of encapsulant materials, and the overall mechanical response of device upon loading and unloading are important parameters that need to be studied before implementing the device into a real application. Hence, this Chapter is dedicated to studying the mechanical

response of fabricated 3D sensors using an indenter equipped with a flat punch probe. Polymers with different stiffness were used for the encapsulation to study the load-bearing and stiffness effect. The structures were mechanically tested under cyclic compressive loading up to 10 and 20% compression. The selected structures were then tested for multiple cycles of loading and at different loading rates for further investigation of durability and viscoelastic effects.

4.2 Materials and methods

Device fabrication started with transfer printing of the Si-NMs from silicon on an insulator wafer (SOI) onto another substrate composed of a layer of PI on a layer of PMMA, both resting on a glass slide. The p-doped (boron) Si-NM piezoresistive elements were formed on the SOI using impurity diffusion. The Si-NM piezoresistors were positioned on the leg-membrane connections of the Table structure. These positions were found to be the optimum locations for sensing of different external mechanical stimuli. The patterning of 2D precursors started with photolithography followed by reactive ion etching to form the silicon elements, and then electron beam evaporation (Cr/Au) to form the metal interconnects for the elements. The formation of 2D precursors were then completed by coating a thin passivation layer of PI. The underlayer PMMA was then dissolved in acetone to enable the transfer of 2D precursors onto a prestretched silicone elastomer substrate using a PDMS stamp.

The geometrical transformation from 2D to 3D configuration was accomplished by the release of the prestrain in the substrate. Finally, the fabrication was completed by encapsulating the entire structure with a thin coating of different polymers, namely

polydimethylsiloxane (PDMS), Ecoflex, and Dragon Skin. The selection of these polymers was based on the difference in their modulus. The Ecoflex and Dragon Skin have a modulus of 68.9 kPa and 151.68 kPa, respectively. PDMS has a modulus of about 1 MPa. Therefore, PDMS had the highest modulus among the polymers. The structures are composed of PI (with modulus of 2.5 GPa) and Gold (with modulus of 76 GPa). Gold has a thickness of 100 nm and is sandwiched between the top PI (with thickness of 2 μm) and bottom polyimide (with thickness of 3 μm). Optical images of plain and encapsulated structures are shown in **Figure 21**. The plain refers to the structure without encapsulation. Note that the encapsulation will not only physically protect the 3D device but also helps to maintain the deformability. The design of the 3D geometry and the type of material utilized for the encapsulation could be optimized for achieving the desired sensitivity [45].

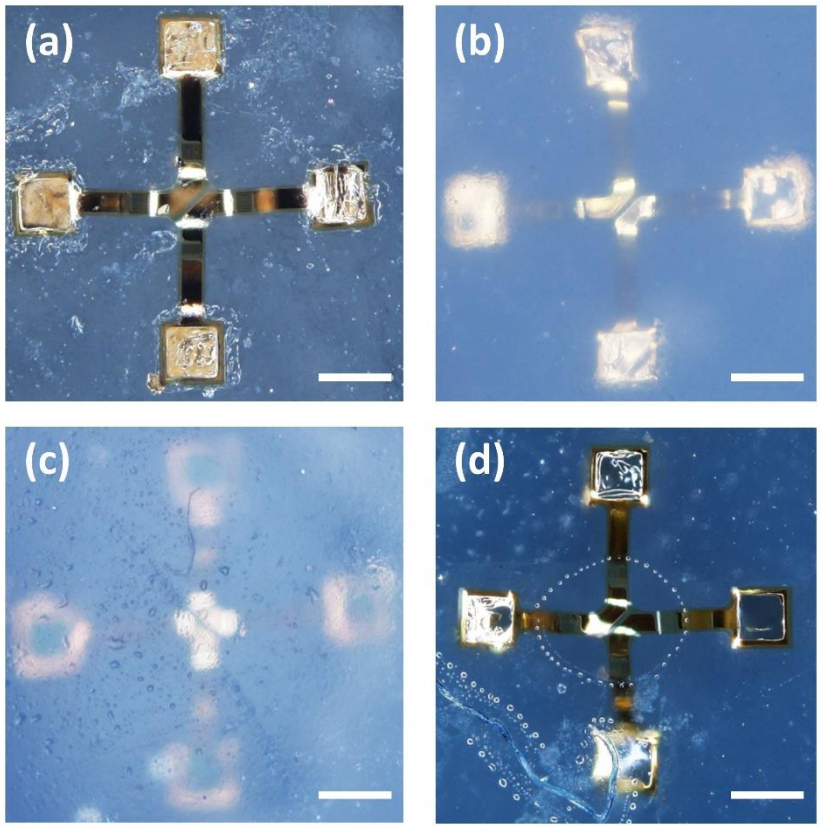

Figure 21. Optical microscopy images of structures (a) without encapsulation, or plain structure, and structures encapsulated with (b) Dragon Skin, (c) Ecoflex, and (d) PDMS (the scale bar is 200 μm).

The structures were initially cyclically compressed to 10 and 20% of their initial height using an instrumented nanoindenter (TI 980, Bruker) equipped with a flat punch probe with a diameter of 100 μm. Displacement-controlled mode was used to compress the structures. Subsequently, selected structures (Ecoflex and PDMS) were compressed to 20% for a large number of cycles and higher loading rates as well to study the durability, hysteresis, and viscoelastic effects when the structures are imposed to a large number of cycles. Note that the experiments in this Chapter could not be performed inside the SEM due to degradation of the encapsulant material. In addition, the encapsulation hindered the

visibility of the structure under it and we were not able to locate the structure to perform the compression.

4.3 Results and discussion

Figure 22(a, b) shows the load-displacement curves for cycling of the Plain structure at 10 and 20% compression. Five sets of cycling experiments were carried out for 10% compression each set consisting of 20 cycles resulting in a total number of 100 cycles. For compression at 20%, three sets of cycling experiments were carried out, each set being 10 cycles resulting in a total number of 30 cycles. All experiments were performed with a constant loading rate of 5μm/s. After the complete unloading of the structure at the end of each set, the next cycle was performed after 4 minutes to allow for the viscous relaxation of the structure and substrate. The punch was fully removed from the structure at the last cycle of each set.

From **Figure 22(a)**, cycling of the structure at 10% was fully elastic with minimal hysteresis. The hysteresis was similar between each set and remained constant for the whole set of cycling tests. Unlike the compression at 10%, cycling at 20% showed different behavior. As shown in **Figure 22(b)**, the load-displacement curves show two regions for the loading associated with Hookean-type deformation with a linear slope and a reduction in the slope due to small buckling of the legs. Similar behavior was observed during the unloading. **Figure 22(d)** shows the changes in the height of the structure measured across the red dashed line shown in **Figure 22(c)**. From the figure, the height of the structure remained unchanged, which shows the full recovery of the structure after cycling to 10 and 20% compression.

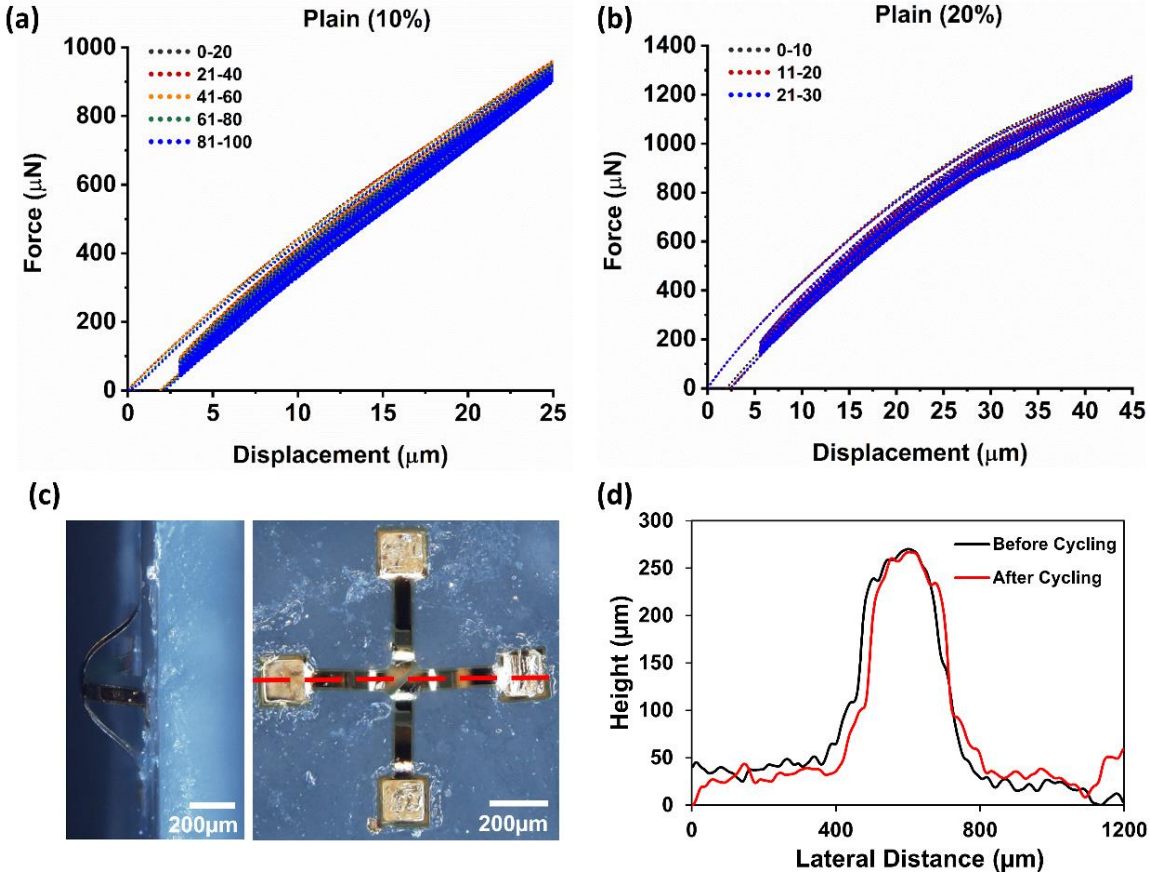

Figure 22. Load–displacement curves for cycling of Plain structure at (a) 10% compression, and (b) 20% compression. (c) the optical images of the structure showing the height of 250μm, and (d) change in the height of the structure before and after cycling.

Figure 23(a, b) shows the load-displacement curves for cycling of structure encapsulated with Dragon Skin at 10 and 20% compression, respectively. The number of cycles and the experimental methods were the same as Plain structure (i.e., 100 cycles at 10% for five sets and 30 cycles at 20% for three sets). Encapsulating the structure with Ecofelx reduced the hysteresis compared with the plain structure, and retained the Hookean behavior even at 20% compression. Compressing the structure to 20% increased the load-bearing capacity by 69%. Compared to plain structure, the load-bearing increased

by 27% once compressed to 10%. The structure maintained minimal and stable hysteresis by increasing the number of cycles. The hysteresis, recovery, and energy dissipation remained the same between each test set for both 10 and 20% compression.

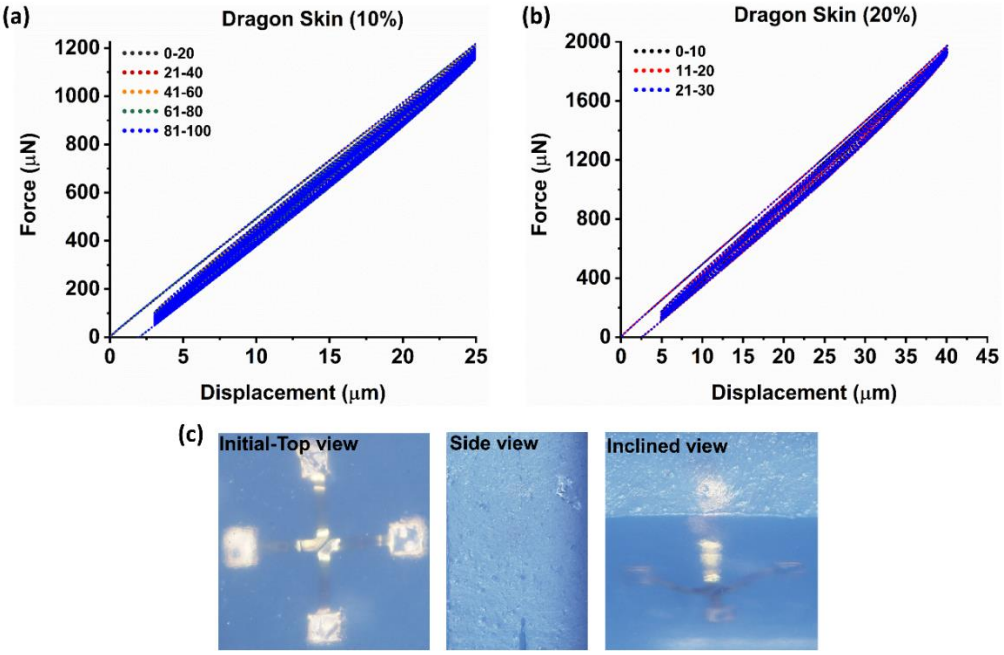

Figure 23. Load–displacement curves for cycling of structure encapsulated with Dragon Skin at (a) 10% compression, and (b) 20% compression, and (c) the optical images of the structure at different positions.

Figure 24(a, b) shows the load-displacement curves for cycling of structure encapsulated with Ecoflex at 10 and 20% compression, respectively. The structure behaved elastically with minimal hysteresis at both 10 and 20% compression for all sets of cycling. Encapsulating the structure with Ecofelx reduced the load-bearing by 58% compared with the Plain structure. Therefore, the entire device softened after encapsulation.

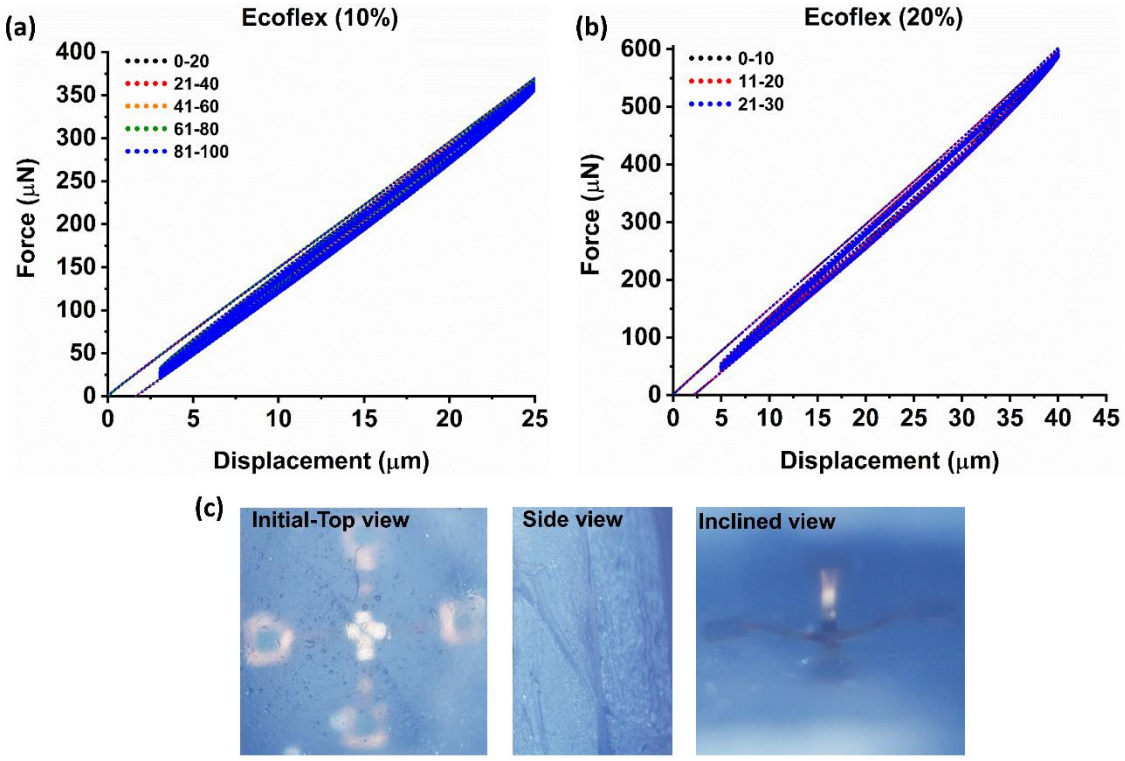

Figure 24. Load–displacement curves for cycling of structure encapsulated with Ecoflex at (a) 10% compression, and (b) 20% compression, and (c) the optical images of the structure at different positions.

Figure 25(a, b) shows the load-displacement curves for cycling of the structure encapsulated with PDMS at 10 and 20% compression, respectively. The structure showed a perfectly elastic behavior and minimum hysteresis among all the structures at both 10 and 20% compression. Encapsulating the structure with PDMS markedly increased the load-bearing by 212% compared with the Plain structure. Therefore, the entire device stiffened after encapsulation.

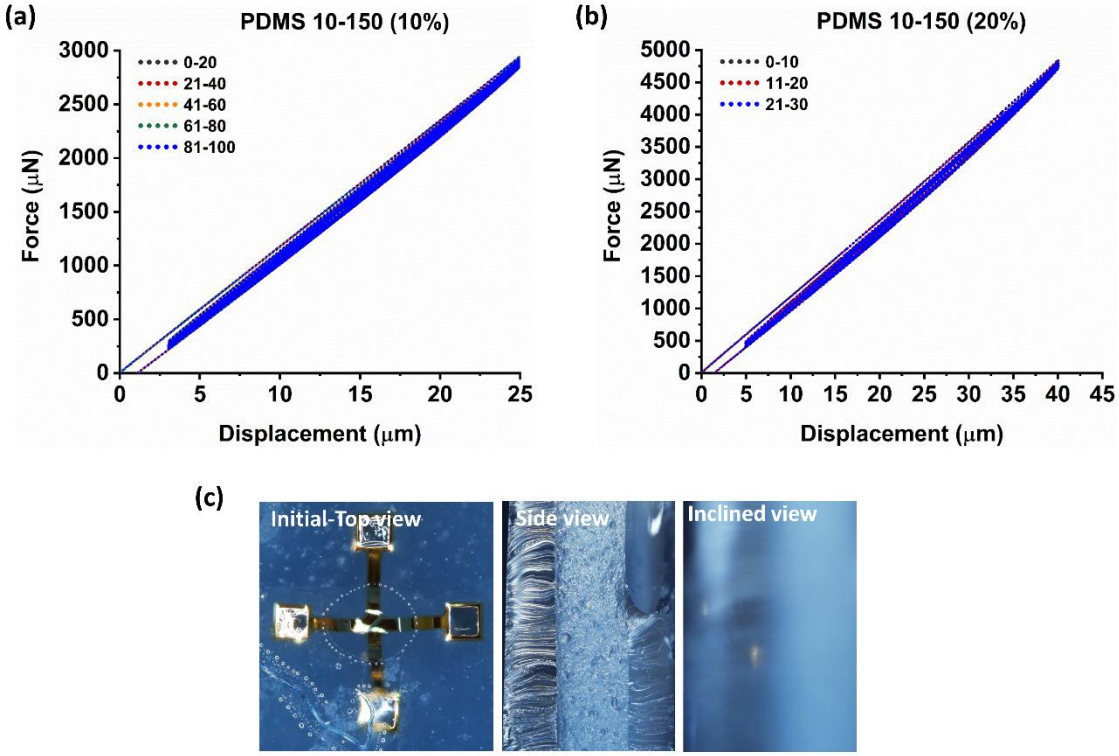

Figure 25. Load–displacement curves for cycling of structure encapsulated with PDMS at (a) 10% compression, and (b) 20% compression, and (c) the optical images of the structure at different positions.

Figure 26(a-c) shows the response (i.e., stiffness and load-bearing capacity) of all structures to the mechanical loading for 10 and 20% compression. The stiffness results (**Figure 26(a, b)**) show negligible variation of stiffness within each set of cycling at both 10 and 20% compression, showing the minimum effect of viscoelasticity of the encapsulant and good durability of the entire structures. The structure encapsulated with PDMS demonstrated the maximum stiffness while Ecoflex reduced the stiffness even with a lower value than plain structure.

Figure 26(c) depicts the comparison of the load-bearing capacity of the structures with and without encapsulation. For each structure, increasing the compression to 20%

resulted in an increase in the maximum load-bearing capacity. The maximum increase occurred for the structure encapsulated with PDMS. Similar to stiffness results, the load-bearing capacity increased for PDMS and Dragon Skin compared to Plain structure, while Ecoflex reduced the value at both 10 and 20% compression. Depending on the ultimate desired sensitivity for the intended application, one could select either of the encapsulant materials for achieving the desired stiffness, load-bearing, and deformation behavior. Herein, for further analysis, we selected the PDMS and Ecoflex, which respectively changed the stiffness and load bearing to maximum and minimum values compared to the Plain structure.

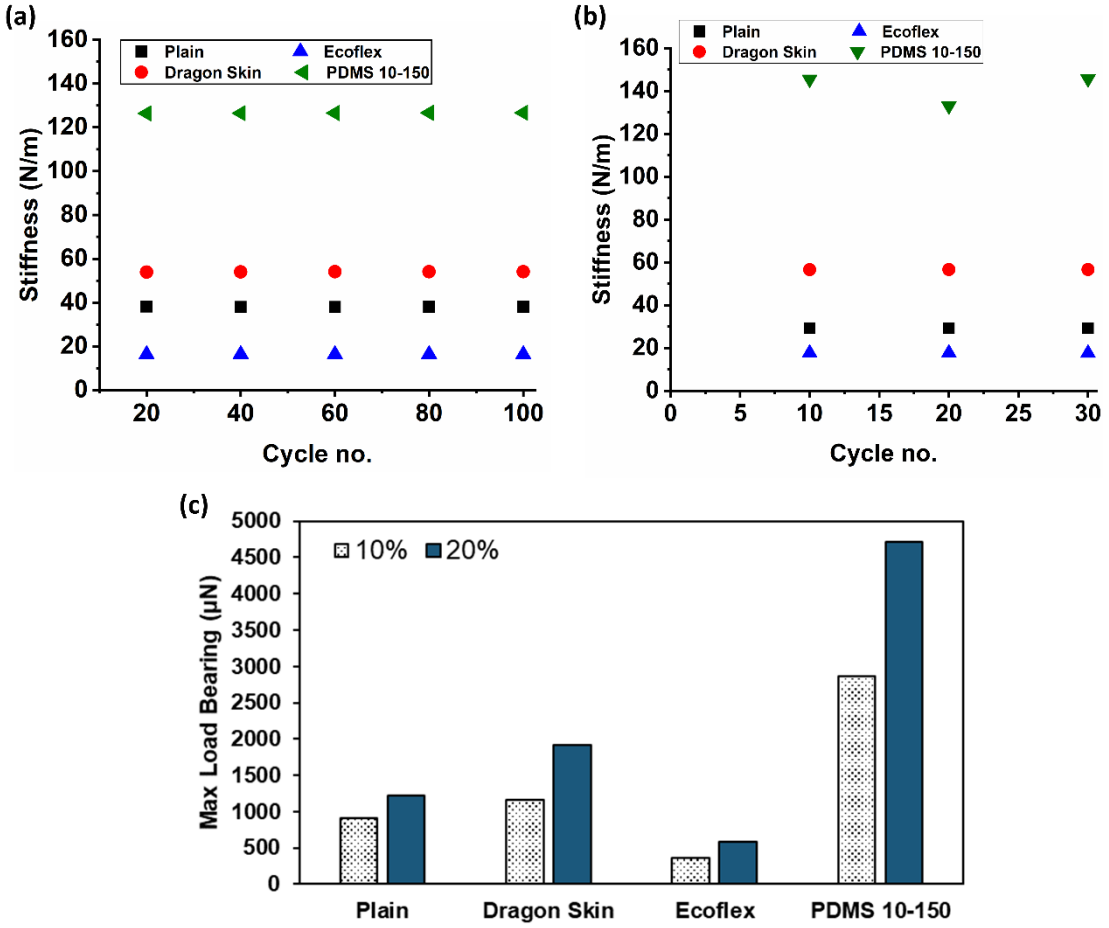

Figure 26. (a, b) Variation of the device stiffness with number of cycles for 10% and 20% compression, respectively, and (c) variations of device load-bearing capacity for different encapsulation materials.

The implementation of these 3D structures into applications such as pressure sensors requires a high level of durability and minimal hysteresis (energy dissipation) against cyclic loading/deformation. Therefore, mechanical deformation needs to be investigated against many cycles of loading/unloading. To this end, Table structures encapsulated with Ecoflex and PDMS were selected for mechanical cycling tests at 20% compression. Each sample was compressed for 500 and 1000 cycles. Experiments with

500 cycles performed with a loading rate of 15 μm/s, while 1000 cycles were performed at a higher frequency of f = 1 Hz, which is similar to human walking frequency.

Figure 27(a, b) shows the load-displacement curves for cycling of structure encapsulated with Ecoflex and PDMS, respectively. Increasing the number of cycles to 500 and 1000 did not alter the hysteresis behavior compared to low cycling tests, and the structures maintained their durable behavior with minimal energy dissipation for both Ecoflex and PDMS encapsulant. Moreover, the structures' hysteresis was found to be insensitive to the loading rate up to f=1Hz. **Figure 27(c, d)** shows the mechanical properties such as load-bearing capacity and stiffness, respectively that were extracted from the load-displacement curves. From **Figure 27(c)**, the variation of maximum load-bearing with the number of cycles and loading rate was found to be negligible for Ecoflex, while for PDMS, the load-bearing slightly decreased with increase of the number of cycles and loading rate by 6 and 10%, respectively. The stiffness followed similar behavior (see **Figure 27(d)**) ad the load-bearing. The stiffness of Ecoflex remain nearly unchanged, whereas the stiffness of PDMS reduced with increase of the number of cycles and loading rate by 10 and 11%, respectively. In summary, the effect of viscoelastic behavior is more pronounced for PDMS compared to Ecoflex.

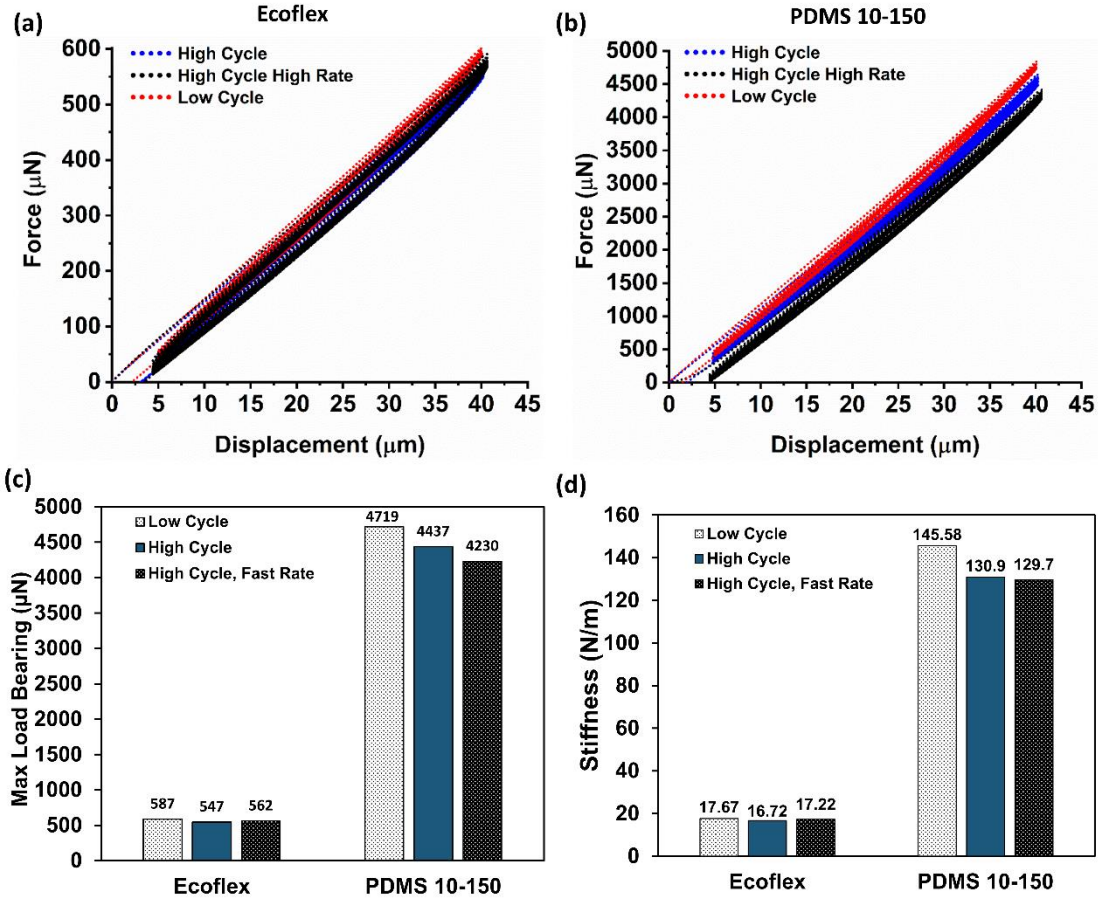

Figure 27. Load-displacement curves for cycling of structures encapsulated with (a) Ecoflex, and (b) PDMS. The calculated mechanical properties were obtained from the load-displacement curves: (c) maximum load-bearing and (d) stiffness at 20% compression.

4.4 Summary

3D kirigami microstructures were fabricated with Table-like geometrical configurations from PI polymer using compressive buckling method. The device was encapsulated with polymers with different stiffnesses, and their mechanical response was measured at 10 and 20% compression under cyclic loading. The experiments were performed with a nanoindenter equipped with a flat punch probe. The goal was to evaluate

the stability and durability of the device against many cycles of loading, the frequency of applied external stimuli, the viscoelastic effect and the load-bearing capability of encapsulant materials. The plain structures showed softening behavior above 10 % compression. Encapsulating the structures minimized the hysteresis. All the encapsulated structures showed a linear elastic behavior at 10 and 20 % compression. The experimental findings indicated the strong effect of encapsulant material on the ultimate mechanical behavior of 3D device. The Ecoflex was found to decrease the load-bearing and stiffness of the device compared to plain structure, while Dragon Skin and particularly PDMS increased the load-bearing and stiffness. Similar to low cycling tests, all the encapsulated structures maintained their durable behavior with minimal energy dissipation upon cycling test to 1000 cycles. The effect of viscoelastic behavior was found to be more pronounced for PDMS compared to Ecoflex encapsulant.

5. CONCLUSION AND RECOMMENDATIONS FOR FUTURE WORK

5.1 Conclusions

This thesis was dedicated to the study of fabrication and deformation of three-dimensional (3D) Kirigami-inspired polymer-based micro-structures made using mechanically-guided 3D micro-assembly. The mechanical response of assembled 3D buckled kirigami structures were investigated through mechanical cyclic and single loading compression and based on the findings, the following conclusions could be drawn:

1) In Chapter 2, the mechanical cycling of 3D structures with different types of structural defects under compressive loading up to 50 and 100% were performed for 3D structures made of SU8. Reduction in load-bearing capacity, energy dissipation, degree of plastic deformation, and overall deformation of the structures were found to be a function of the defect type. Despite the defect type, all structures ultimately achieved stable hysteresis with steady-state mechanical behavior at compression of 50% and extreme condition of 100 %, which is advantageous in practical applications as in flexible and stretchable electronics.
2) In chapter 3, the 3D structures consisted of a layer of E44 shape memory epoxy, which were patterned using microfabrication. The mechanics of these kirigami structures were studied using experimental instrumentation and computational modeling through mechanical cyclic and single loading compression at room and elevated temperatures, respectively. Our findings

reveal that the load-bearing capacity, resilience, and stability under deformation were largely affected by structures' geometry. The SM behavior of the structures was observed inside a scanning electron microscopy, indicating outstanding shape memory behavior by full recovery to their original shape.

3) In Chapter 4, 3D Kirigami microstructures were fabricated with Table-like geometrical configurations from PI polymer integrated with piezoresistive elements. The device was encapsulated with polymers with different stiffnesses, and their mechanical response was measured at 10 and 20% compression under cyclic loading. All the encapsulated structures showed a linear elastic behavior, while Plain structure softened after 10% compression. The Ecoflex and PDMS were found to respectively decrease and increase the load-bearing and stiffness of the device compared to Plain structure.

5.2 Recommendations for Future Work

As seen in Chapter 2, the mechanical response of the structures was found to be dependent on the defect type. The FEA showed the stress/strain distribution for each defective structure upon single loading compression. Future studies need to be carried out for modeling of cyclic compression for more precise comparison with the experiments.

In Chapter 3, the shape memory effect was qualitatively captured inside the SEM. However, due to the high transition temperature and sample dimensions, we were not able to get the thermo-mechanical force-displacement diagram. Future studies could be focused on developing the recipe for body temperature SMPs to fabricate 3D structures in

micron scales. Further studies could be carried out to investigate the time-dependent properties such as strain rate sensitivity, and stress relaxation and creep testing. Moreover, there has not been a lot of work with shear/sliding of these structures, which is a potential area for further studies.

In Chapter 4, the 3D structures were integrated with piezoresistive elements and encapsulated with polymers with different stiffness to fabricate 3D tactile pressure sensor. Due to degradation of encapsulant polymers inside the SEM and invisibility of the structures, we were not able to see the deformation of the structure. Further studies could be focused on resolving this issue. For example, one could attach the encapsulant material to the flat punch and compress the Plain structure inside the SEM.

REFERENCES

[1] Yan Z, Han M, Yang Y, Nan K, Luan H, Luo Y, et al. Deterministic assembly of 3D mesostructures in advanced materials via compressive buckling: A short review of recent progress. Extrem Mech Lett 2017;11:96–104. doi:10.1016/J.EML.2016.12.006.

[2] Xu S, Yan Z, Jang K, Huang W, Fu H, … JK-, et al. Assembly of micro/nanomaterials into complex, three-dimensional architectures by compressive buckling. Science 2015;347:154–9. doi:10.1126/science.1260960.

[3] Fan Z, Razavi H, Do JW, Moriwaki A, Ergen O, Chueh YL, et al. Three-dimensional nanopillar-array photovoltaics on low-cost and flexible substrates. Nat Mater 2009;8:648–53. doi:10.1038/nmat2493.

[4] Braun P V. Materials chemistry in 3D templates for functional photonics. Chem Mater 2014;26:277–86. doi:10.1021/cm4023437.

[5] Leong TG, Randall CL, Benson BR, Bassik N, Stern GM, Gracias DH. Tetherless thermobiochemically actuated microgrippers. Proc Natl Acad Sci U S A 2009;106:703–8. doi:10.1073/pnas.0807698106.

[6] Yu M, Huang Y, Ballweg J, Shin H, Huang M, Savage DE, et al. Semiconductor nanomembrane tubes: Three-dimensional confinement for controlled neurite outgrowth. ACS Nano 2011;5:2447–57. doi:10.1021/nn103618d.

[7] Gansel JK, Thiel M, Rill MS, Decker M, Bade K, Saile V, et al. Gold helix photonic metamaterial as broadband circular polarizer. Science 2009;325:1513–5.

doi:10.1126/science.1177031.

[8] Zheng X, Lee H, Weisgraber TH, Shusteff M, DeOtte J, Duoss EB, et al. Ultralight, ultrastiff mechanical metamaterials. Science 2014;344:1373–7. doi:10.1126/science.1252291.

[9] Zhang H, Yu X, Braun P V. Three-dimensional bicontinuous ultrafast-charge and-discharge bulk battery electrodes. Nat Nanotechnol 2011;6:277–81. doi:10.1038/nnano.2011.38.

[10] Jiang H, Lee PS, Li C. 3D carbon based nanostructures for advanced supercapacitors. Energy Environ Sci 2013;6:41–53. doi:10.1039/c2ee23284g.

[11] Wood RJ. The challenge of manufacturing between Macro and Micro: classic ways of folding paper into dynamic shapes--origami, pop-up books--inspire methods to engineer millimeter-scale machines. Am Sci 2014;102:124–32.

[12] Rogers J, Huang Y, Schmidt OG, Gracias DH. Origami MEMS and NEMS. MRS Bull 2016;41:123–9. doi:10.1557/mrs.2016.2.

[13] Yan Z, Zhang F, Wang J, Liu F, Guo X, Nan K, et al. Controlled Mechanical Buckling for Origami-Inspired Construction of 3D Microstructures in Advanced Materials. Adv Funct Mater 2016;26:2629–39. doi:10.1002/adfm.201504901.

[14] Fu H, Nan K, Bai W, Huang W, Bai K, Lu L, et al. Morphable 3D mesostructures and microelectronic devices by multistable buckling mechanics. Nat Mater 2018;17:268–76. doi:10.1038/s41563-017-0011-3.

[15] Li S, Han M, Rogers JA, Zhang Y, Huang Y, Wang H. Mechanics of buckled serpentine structures formed via mechanics-guided, deterministic three-

dimensional assembly. J Mech Phys Solids 2019;125:736–48. doi:10.1016/j.jmps.2019.01.019.

[16] Ning X, Wang X, Zhang Y, Yu X, Choi D, Zheng N, et al. Assembly of Advanced Materials into 3D Functional Structures by Methods Inspired by Origami and Kirigami: A Review. Adv Mater Interfaces 2018;5:1800284. doi:10.1002/admi.201800284.

[17] Ray TR, Choi J, Bandodkar AJ, Krishnan S, Gutruf P, Tian L, et al. Bio-integrated wearable systems: A comprehensive review. Chem Rev 2019;119:5461–533. doi:10.1021/acs.chemrev.8b00573.

[18] Humood M, Shi Y, Han M, Lefebvre J, Yan Z, Pharr M, et al. Fabrication and Deformation of 3D Multilayered Kirigami Microstructures. Small 2018;14:1703852. doi:10.1002/smll.201703852.

[19] Humood M, Lefebvre J, Shi Y, Han M, Fincher CD, Pharr M, et al. Fabrication and Mechanical Cycling of Polymer Microscale Architectures for 3D MEMS Sensors. Adv Eng Mater 2019;21:1801254. doi:10.1002/adem.201801254.

[20] Wang C, Taherabadi L, Jia G, Madou M, Yeh Y, Dunn B. C-MEMS for the Manufacture of 3D Microbatteries. Electrochem Solid-State Lett 2004;7:A435. doi:10.1149/1.1798151.

[21] Felton S, Tolley M, Demaine E, Rus D, Wood R. A method for building self-folding machines Downloaded from. Science 2014;345:644–6. doi:10.1126/science.1252610.

[22] Randall CL, Gultepe E, Gracias DH. Self-folding devices and materials for

biomedical applications. Trends Biotechnol 2012;30:138–46. doi:10.1016/J.TIBTECH.2011.06.013.

[23] Tian B, Liu J, Dvir T, Jin L, Tsui JH, Qing Q, et al. Macroporous nanowire nanoelectronic scaffolds for synthetic tissues. Nat Mater 2012;11:986–94. doi:10.1038/nmat3404.

[24] Song Z, Ma T, Tang R, Cheng Q, Wang X, Krishnaraju D, et al. Origami lithium-ion batteries. Nat Commun 2014;5:3140. doi:10.1038/ncomms4140.

[25] Lukatskaya MR, Dunn B, Gogotsi Y. Multidimensional materials and device architectures for future hybrid energy storage. Nat Commun 2016;7:12647. doi:10.1038/ncomms12647.

[26] Rogers JA, Someya T, Huang Y. Materials and mechanics for stretchable electronics. Science 2010;327:1603–7. doi:10.1126/science.1182383.

[27] Su Y, Ping X, Yu KJ, Lee JW, Fan JA, Wang B, et al. In-Plane Deformation Mechanics for Highly Stretchable Electronics. Adv Mater 2017;29:1604989. doi:10.1002/adma.201604989.

[28] Breger JC, Yoon C, Xiao R, Kwag HR, Wang MO, Fisher JP, et al. Self-Folding Thermo-Magnetically Responsive Soft Microgrippers. ACS Appl Mater Interfaces 2015;7:3398–405. doi:10.1021/am508621s.

[29] Schumann M, Bückmann T, Gruhler N, Wegener M, Pernice W. Hybrid 2D–3D optical devices for integrated optics by direct laser writing. Light Sci Appl 2014;3:e175. doi:10.1038/lsa.2014.56.

[30] Silverberg JL, Evans AA, Mcleod L, Hayward RC, Hull T, Santangelo CD, et al.

Using origami design principles to fold reprogrammable mechanical metamaterials. Science 2014;345:647–50. doi:10.1126/science.1252876.

[31] Yan Z, Zhang F, Liu F, Han M, Ou D, Liu Y, et al. Mechanical assembly of complex, 3D mesostructures from releasable multilayers of advanced materials. Sci Adv 2016:e1601014. doi:10.1126/sciadv.1601014.

[32] Iannacci J. Reliability of MEMS: A perspective on failure mechanisms, improvement solutions and best practices at development level. Displays 2015;37:62–71. doi:10.1016/J.DISPLA.2014.08.003.

[33] Mulloni V, Margesin B, Farinelli P, Marcelli R, Lucibello A, De Angelis G. Cycling reliability of RF-MEMS switches with Gold–Platinum multilayers as contact material. Microsyst Technol 2017;23:3843–50. doi:10.1007/s00542-015-2782-2.

[34] Pini V, Ruz JJ, Kosaka PM, Malvar O, Calleja M, Tamayo J. How two-dimensional bending can extraordinarily stiffen thin sheets. Sci Rep 2016;6:29627. doi:10.1038/srep29627.

[35] Vasudevan A., Sadananda K. Analysis of fatigue crack growth under compression–compression loading. Int J Fatigue 2001;23:365–74. doi:10.1016/S0142-1123(01)00172-4.

[36] Liu K, Jiang L. Bio-inspired design of multiscale structures for function integration. Nano Today 2011;6:155–75. doi:10.1016/J.NANTOD.2011.02.002.

[37] Zhao N, Wang Z, Cai C, Shen H, Liang F, Wang D, et al. Bioinspired Materials: from Low to High Dimensional Structure. Adv Mater 2014;26:6994–7017.

doi:10.1002/adma.201401718.

[38] Ahn J-H, Kim H-S, Lee KJ, Jeon S, Kang SJ, Sun Y, et al. Heterogeneous Three-Dimensional Electronics by Use of Printed Semiconductor Nanomaterials. Science 2006;314:1754–7. doi:10.1126/science.1132394.

[39] Xu L, Gutbrod SR, Bonifas AP, Su Y, Sulkin MS, Lu N, et al. 3D multifunctional integumentary membranes for spatiotemporal cardiac measurements and stimulation across the entire epicardium. Nat Commun 2014;5:3329. doi:10.1038/ncomms4329.

[40] Liu Z, Qi D, Leow WR, Yu J, Xiloyannnis M, Cappello L, et al. 3D-Structured Stretchable Strain Sensors for Out-of-Plane Force Detection. Adv Mater 2018;30:1707285. doi:10.1002/adma.201707285.

[41] Tian B, Liu J, Dvir T, Jin L, Tsui JH, Qing Q, et al. Macroporous nanowire nanoelectronic scaffolds for synthetic tissues. Nat Mater 2012;11:986–94. doi:10.1038/nmat3404.

[42] Feiner R, Engel L, Fleischer S, Malki M, Gal I, Shapira A, et al. Engineered hybrid cardiac patches with multifunctional electronics for online monitoring and regulation of tissue function. Nat Mater 2016;15:679–85. doi:10.1038/nmat4590.

[43] Liu X, Yuk H, Lin S, Parada GA, Tang T-C, Tham E, et al. 3D Printing of Living Responsive Materials and Devices. Adv Mater 2018;30:1704821. doi:10.1002/adma.201704821.

[44] Song Z, Ma T, Tang R, Cheng Q, Wang X, Krishnaraju D, et al. Origami lithium-ion batteries. Nat Commun 2014;5:3140. doi:10.1038/ncomms4140.

[45] Han M, Wang H, Yang Y, Liang C, Bai W, Yan Z, et al. Three-dimensional piezoelectric polymer microsystems for vibrational energy harvesting, robotic interfaces and biomedical implants. Nat Electron 2019;2:26–35. doi:10.1038/s41928-018-0189-7.

[46] Soukoulis CM, Wegener M. Past achievements and future challenges in the development of three-dimensional photonic metamaterials. Nat Photonics 2011;5:523–30. doi:10.1038/nphoton.2011.154.

[47] Overvelde JTB, Weaver JC, Hoberman C, Bertoldi K. Rational design of reconfigurable prismatic architected materials. Nature 2017;541:347–52. doi:10.1038/nature20824.

[48] Yan Z, Han M, Shi Y, Badea A, Yang Y, Kulkarni A, et al. Three-dimensional mesostructures as high-temperature growth templates, electronic cellular scaffolds, and self-propelled microrobots. Proc Natl Acad Sci U S A 2017;114:E9455–64. doi:10.1073/pnas.1713805114.

[49] Breger JC, Yoon C, Xiao R, Kwag HR, Wang MO, Fisher JP, et al. Self-Folding Thermo-Magnetically Responsive Soft Microgrippers. ACS Appl Mater Interfaces 2015;7:3398–405. doi:10.1021/am508621s.

[50] Rogers J, Huang Y, Schmidt OG, Gracias DH. Origami MEMS and NEMS. MRS Bull 2016;41:123–9. doi:10.1557/mrs.2016.2.

[51] Lin D, Nian Q, Deng B, Jin S, Hu Y, Wang W, et al. Three-Dimensional Printing of Complex Structures: Man Made or toward Nature? ACS Nano 2014;8:9710–5. doi:10.1021/nn504894j.

[52] Moon JH, Ford J, Yang S. Fabricating three-dimensional polymeric photonic structures by multi-beam interference lithography. Polym Adv Technol 2006;17:83–93. doi:10.1002/pat.663.

[53] Farsari M, Chichkov BN. Two-photon fabrication. Nat Photonics 2009;3:450–2. doi:10.1038/nphoton.2009.131.

[54] Zhang X, Pint CL, Lee MH, Schubert BE, Jamshidi A, Takei K, et al. Optically- and Thermally-Responsive Programmable Materials Based on Carbon Nanotube-Hydrogel Polymer Composites. Nano Lett 2011;11:3239–44. doi:10.1021/nl201503e.

[55] Yan Z, Zhang F, Liu F, Han M, Ou D, Liu Y, et al. Mechanical assembly of complex, 3D mesostructures from releasable multilayers of advanced materials. Sci Adv 2016;2:e1601014. doi:10.1126/sciadv.1601014.

[56] Zhang Y, Yan Z, Nan K, Xiao D, Liu Y, Luan H, et al. A mechanically driven form of Kirigami as a route to 3D mesostructures in micro/nanomembranes. Proc Natl Acad Sci U S A 2015;112:11757–64. doi:10.1073/pnas.1515602112.

[57] Wang X, Guo X, Ye J, Zheng N, Kohli P, Choi D, et al. Freestanding 3D Mesostructures, Functional Devices, and Shape-Programmable Systems Based on Mechanically Induced Assembly with Shape Memory Polymers. Adv Mater 2019;31:1805615. doi:10.1002/adma.201805615.

[58] Guo X, Xu Z, Zhang F, Wang X, Zi Y, Rogers JA, et al. Reprogrammable 3D Mesostructures Through Compressive Buckling of Thin Films with Prestrained Shape Memory Polymer. Acta Mech Solida Sin 2018;31:589–98.

doi:10.1007/s10338-018-0047-1.

[59] Humood M, Lefebvre J, Shi Y, Han M, Fincher CD, Pharr M, et al. Fabrication and Mechanical Cycling of Polymer Microscale Architectures for 3D MEMS Sensors. Adv Eng Mater 2019;21:1801254. doi:10.1002/adem.201801254.

[60] Yu K, Ge Q, Qi HJ. Reduced time as a unified parameter determining fixity and free recovery of shape memory polymers. Nat Commun 2014;5:3066. doi:10.1038/ncomms4066.

[61] Santhosh Kumar KS, Biju R, Reghunadhan Nair CP. Progress in shape memory epoxy resins. React Funct Polym 2013;73:421–30. doi:10.1016/j.reactfunctpolym.2012.06.009.

[62] Zhao W, Liu L, Zhang F, Leng J, Liu Y. Shape memory polymers and their composites in biomedical applications. Mater Sci Eng C 2019;97:864–83. doi:10.1016/j.msec.2018.12.054.

[63] Liu Y, Du H, Liu L, Leng J. Shape memory polymers and their composites in aerospace applications: A review. Smart Mater Struct 2014;23:023001. doi:10.1088/0964-1726/23/2/023001.

[64] Toyama S, Tanaka Y, Shirogane S, Nakamura T, Umino T, Uehara R, et al. Development of Wearable Sheet-Type Shear Force Sensor and Measurement System that is Insusceptible to Temperature and Pressure. Sensors 2017;17:1752. doi:10.3390/s17081752.

[65] Hua Q, Sun J, Liu H, Bao R, Yu R, Zhai J, et al. Skin-inspired highly stretchable and conformable matrix networks for multifunctional sensing. Nat Commun

2018;9:1–11. doi:10.1038/s41467-017-02685-9.

[66] You I, Choi S-E, Hwang H, Han SW, Kim JW, Jeong U. E-Skin Tactile Sensor Matrix Pixelated by Position-Registered Conductive Microparticles Creating Pressure-Sensitive Selectors. Adv Funct Mater 2018;28:1801858. doi:10.1002/adfm.201801858.

[67] Gao Y, Ota H, Schaler EW, Chen K, Zhao A, Gao W, et al. Wearable Microfluidic Diaphragm Pressure Sensor for Health and Tactile Touch Monitoring. Adv Mater 2017;29. doi:10.1002/adma.201701985.

[68] Liu Y, Wang H, Zhao W, Zhang M, Qin H, Xie Y. Flexible, Stretchable Sensors for Wearable Health Monitoring: Sensing Mechanisms, Materials, Fabrication Strategies and Features. Sensors 2018;18:645. doi:10.3390/s18020645.

[69] Won SM, Wang H, Kim BH, Lee K, Jang H, Kwon K, et al. Multimodal Sensing with a Three-Dimensional Piezoresistive Structure. ACS Nano 2019;13:10972–9. doi:10.1021/acsnano.9b02030.

[70] Ning X, Wang H, Yu X, Soares JANT, Yan Z, Nan K, et al. 3D Tunable, Multiscale, and Multistable Vibrational Micro-Platforms Assembled by Compressive Buckling. Adv Funct Mater 2017;27:1605914. doi:10.1002/adfm.201605914.

[71] Truby RL, Lewis JA. Printing soft matter in three dimensions. Nature 2016;540:371–8. doi:10.1038/nature21003.

[72] Cumpston BH, Ananthavel SP, Barlow S, Dyer DL, Ehrlich JE, Erskine LL, et al. Two-photon polymerization initiators for three-dimensional optical data storage and microfabrication. Nature 1999;398:51–4. doi:10.1038/17989.

[73] Chen Z, Huang G, Trase I, Han X, Mei Y. Mechanical Self-Assembly of a Strain-Engineered Flexible Layer: Wrinkling, Rolling, and Twisting. Phys Rev Appl 2016;5:017001. doi:10.1103/PhysRevApplied.5.017001.